Department of Physics and Astronomy
Heidelberg University

Bachelor Thesis in Physics
submitted by

Lea Maria Luca Neumann

born in Kassel (Germany)

2024

Theoretical investigation of the superfluid-supersolid phase transition of a 3D dysprosium quantum gas

This Bachelor Thesis has been carried out by Lea Maria Luca Neumann at the
Physikalisches Institut in Heidelberg
under the supervision of
Prof. Lauriane Chomaz

Theoretical investigation of the superfluid-supersolid phase transition of a 3D dysprosium quantum gas

In this thesis, the three dimensional dysprosium quantum gas in the framework of the DyLab experiment in Heidelberg is simulated by solving the extended Gross-Pitaevskii equation. The ground states of the quantum gas are simulated at different s-wave scattering lengths a_s to analyze the superfluid-supersolid phase transition. The ground states are analyzed by calculating the one dimensional density contrast with two different methods, to then determine the order of the phase transition. With the chosen geometry the phase transition was found to be discontinuous with a finite sized gap in the density contrast of $\Delta\mathcal{C} = 0.458$. In a second part the phase transition is simulated by linearly quenching the scattering length a_s in a dynamical simulation. Two different quenches are applied. This is then compared to the results from the ground state simulations. The systems final state is different from the calculated ground state for both simulated quenches. In both ground state and dynamical simulations, a strong competition between forming a 1D and 2D crystal is found.

Theoretische Untersuchung des suprafluid-suprasolid Phasenübergangs eines 3D Dysprosium Quantengas

In dieser Arbeit wird das dreidimensionale bosonische Dysprosium-Quantengas im Rahmen des DyLab-Experiments in Heidelberg durch Lösen der extended Gross-Pitaevskii-Gleichung simuliert. Die Grundzustände des Quantengases werden bei verschiedenen s-Wellenstreulängen a_s simuliert, um den Phasenübergang superfluid-supersolid zu analysieren. Die Grundzustände werden durch Berechnung des eindimensionalen Dichtekontrasts mit zwei verschiedenen Methoden analysiert, um dann die Ordnung des Phasenübergangs zu bestimmen. Es wurde ein diskontinuierlicher Phasenübergang für die gewählte Geometrie des Systems gefunden. Der endliche Sprung im Dichtekontrast ist dafür $\Delta\mathcal{C} = 0,458$. In einem zweiten Teil wird der Phasenübergang durch lineares Quenchen der Streulänge a_s in einer dynamischen Simulation simuliert. Dies wird dann mit den Ergebnissen aus den Grundzustandssimulationen verglichen. Der Endzustand des Systems unterscheidet sich vom berechneten Grundzustand für beide simulierten Quenches. Sowohl bei den Grundzustandssimulationen als auch bei den dynamischen Simulationen ist ein starker Wettbewerb zwischen der Bildung eines 1D- und eines 2D-Kristalls festgestellt worden.

Contents

1. Introduction

Quantum fluids have been a playground for physicists to study intriguing quantum phenomena and contributed to understand the quantum world. They are still the center of many more studies to gain knowledge about their bizarre phenomena.

Predicted in 1925 by Einstein [1] after receiving the theoretical calculations of Bose and firstly observed experimentally in 1995 by Ketterle, Wieman and Cornell [2] the Bose-Einstein condensate is the center of quantum fluid experiments. As the Nobel Prize announcement poetically states, "the three physicists 'caused atoms to 'sing in unison' " [2]. The achievement to observe atoms entering the same quantum state, where the matter waves of atoms overlap leading to one single wave function to describe the system was revolutionary and is a pure quantum mechanical effect.

Bose-Einstein condensation relates to another surprising behavior: superfluidity. Superfluidity is a state, which allows the fluid to flow without experiencing viscosity[3]. The term superfluidity was firstly mentioned in 1938 after experiments with liquid ^{4}He in 1938 by Allen, Misener and Kapitza did research on its flow properties [4, 5]. The link between Bose-Einstein condensation was first proposed by F. London [6, 7] and with later theories by Tisza [8], Landau [9] linking superfluidity to a linear dispersion relation, which Bogoliobov then derived as the dispersion relation of interacting quantum Bose gases [10], direct connection between the existence of superfluidity and the BEC was made. Non-interacting particles would not have a linear part in their dispersion and therefore could not have any superfluid properties.

When probing a dipolar quantum gas, another interesting phase, the supersolid phase, is an ongoing topic of interest. Supersolidity is a quantum state which both exhibits crystalline and superfluid properties. These properties require breaking the continuous transnational symmetry for the crystal and the continuous symmetry of phase invariance for a superfluid [11] and the existence of such a phase requires a roton minimum in the energy momentum relation [12]. The concept of supersolidity was first proposed theoretically in the 1960s for ^{4}He and general quantum crystals [13–16], but experimental breakthroughs in preparing this quantum state needed more than 40 years. The first experimental result, where supersolids were indicated, was published in 2004 by Kim and Chan [17]. This experiment used solid helium to find supersolid properties. The experimental results for supersolid helium have been elusive, but later cold atom experiments (2017) conducted at the ETH Zürich [11] and MIT [18] achieved the supersolid state. The difficulty to ensure both phase coherence (superfluid property) and density modulation (solid property) was overcome by using light interactions to have the needed atomic interactions. The Zürich group used optical resonators to create a lattice supersolid with ^{87}Rb atoms and the MIT group used induced spin-orbit coupling to create a stripe modulated sodium supersolid. Later on in 2019, experiments with dysprosium and erbium have confirmed the supersolid phase in dipolar quantum gas experiments [**Modugno**, 19, 20], in which the supersolid behavior is a result of the long-range dipole interactions.

To undergo a phase transition to the supersolid regime, the interactions between the atoms must be sufficiently large and the confinement in the trap has to be anisotropic [12]. Furthermore, to distinguish between the normal solid phase (distinct density and the supersolid phase, the correct trapping potential, relative dipole strength (ratio between dipolar and contact interactions, $\varepsilon_{dd} = a_{dd}/a_s$) and large enough atom number have to be ensured [12]. The transition from the superfluid phase to the supersolid phase is achieved by tuning the s-wave scattering length a_s with magnetic Feshbach resonances. For ^{164}Dy a thermal transition to the supersolid state is also possible because ^{164}Dy has a background scattering length which is smaller than the dipole strength a_{dd}. This allows a transition to the supersolid regime without the use of Feshbach resonances [19].

This thesis aims to further understand the phase transition between the superfluid phase and the supersolid phase with respect to the s-wave scattering length a_s, with having a distinct experimental framework of the DyLab experiment in Heidelberg. The phase transition is analyzed to gain insight into the influence of distinct values of a_s on the ground states. Additionally, the dynamics of a condensate, which is exposed to a linear quench are analyzed to gain insight into the dynamical behavior of the system when crossing the phase transition.

Outline: In this thesis the dysprosium quantum gas from the DyLab in Heidelberg is simulated. The thesis includes the description of the physical background, the numerical methods followed by the results of the ground state and dynamical simulations.

In Chapter 2 the physical concepts underlying this work are explained by introducing the DyLab experiment and the properties of dysprosium to then further focus on ultracold quantum gas theory. This includes Bose-Einstein condensation, the Gross-Pitaevskii equation and Landau theory of phase transitions.

Chapter 3 gives a short introduction of the numerical methods used in the simulation. The imaginary time propagation method and the split-step-Fourier method are outlined. Important for simulations, which include calculations in Fourier space, of particles with long range interactions like dysprosium is the implementation of a cut-off potential, which then is introduced. Finally the chapter ends with the used methods of convergence testing.

In Chapter 4 the dysprosium gas is simulated to find the phase transition between the superfluid phase and the supersolid phase when varying the scattering length a_s. The phase transition is first qualitatively described. To classify the transition the contrast is evaluated for each simulated ground state. The contrast is then compared to the theory of Landau theory for the phase transitions.

Chapter 5 treats dynamical simulations where the scattering length of the quantum gas is linearly quenched over the superfluid-supersolid phase transition. The dynamical states are compared to the calculated ground states and their difference interpreted through the extraction of a response time. The response time of the system is evaluated as well as the final reached state.

The final Chapter 6 will summarize the simulations and results and provide an overall summary of the thesis.

Nota bene: the index notation with the indices i, j, k refer to the dimensions x, y, z but are interchangeable, meaning $x_i = x$ or y or z, depending on the context, which will be clearly stated. The same rule applies to dx_i, dx_j, dx_z. The vector notation generally is chosen to be $\vec{x} \equiv \mathbf{x}$, with the exception of referring to a matrix once. This exception will be stated clearly. Furthermore the variables N' and N are not interchangeable, as the first one refers to the atom total atom number in the condensate fraction and the second one refers to the normalization of the wave function.

2. Physical background

The simulations carried out in this thesis are takes place in the framework of the dysprosium experiment in Heidelberg. The experimental setup is an ultra-cold atom gas experiment, where a dilute Bose-Einstein-condensate and possibly supersolid states are achieved with dysprosium gas. In this chapter the physical basics for this framework are explained.

2.1. The DyLab in Heidelberg

The DyLab in Heidelberg is an ultra-cold atom experiment with dysprosium atoms which is under the supervision of Prof. Lauriane Chomaz. The experiment aims to unveil equilibrium and dynamical behaviors of the quantum fluid, by creating and probing a degenerate dysprosium quantum gas. In the future the dimensionality of the gas is aimed to change from 3D to 2D. The trap to confine the atoms used after the loading stages, is a cross optical dipole trap with $\lambda = 1064$nm, a far red-detuned laser, with linear polarized light. The beam used is a Gaussian beam, which is then modulated to achieve the desired properties. The dipole traps are tunable (by using an acousto-optic deflector, for more information see [21]) and are used in the cooling stage of the experiment as well as for tailoring the atom cloud as desired. In the experiment the trapping frequencies shown in 4.1 are achieved by modulating the Gaussian beam. In the experiment the atom number in the condensed fraction N_{BEC} was measured (also in Tab.4.1). The thermal fraction could not be precisely measured in this measurement. N_{BEC} will further be referenced as N'.

N_{BEC}	$\omega_x[2\pi\text{Hz}]$	$\omega_y[2\pi\text{Hz}]$	$\omega_z[2\pi\text{Hz}]$
$1.24(12) \cdot 10^5$	44.97(12)	10.4(2)	126.3(5)

Table 2.1.: Experimental parameters used in the simulations.

2.2. Dysprosium

Magnetic Lanthanides (Ln) are of great interest for the study of quantum phenomena in the ultra cold range because of their strong dipolar behavior [22]. The lanthanide dysprosium has the atomic number 66 and was first discovered by Paul-Emile Lecoq de Boisbaudron [23]. Dysprosium has several stable isotopes as listed in Table 2.2. In the dysprosium lab in Heidelberg, the most abundant isotope ^{164}Dy is used, but other experiments also use ^{162}Dy or others [24, 25]. The electronic configuration of dysprosium is

$$[Xe]4f^{10}6s^2, \tag{2.1}$$

and with 66 as its atomic number, dysprosium has, as all Ln, a Xenon like core, a closed outer $6s$ shell and an inner open $4f$ shell [22]. In the case of dysprosium, the inner shell contains 10 electrons. The Ln Dy in particular is used, because it has the strongest magnetic moment of all elements in the periodic table with a magnetic dipole moment of $\mu_m = 9.93\mu_B$, with the Bohr magneton μ_B (for the derivation see [26]). This stems from its electronic configuration with 4 uncoupled spins in the f shell. The shown dipole lengths in Tab.2.2 are according to Eq.2.2

Isotope	^{164}Dy	^{162}Dy	^{163}Dy	^{161}Dy	^{160}Dy
Abundance [%]	28.3	25.5	24.9	18.9	$2-3$
Mass [u]	163.93	161.93	162.93	160.93	159.93
Dipole length $a_{dd}[a_0]$	130.7	129.2	130	128.4	127.6
Statistics	boson	boson	fermion	fermion	boson

Table 2.2.: Properties of the most abundant stable dysprosium isotopes. Values extracted from [22, 23].

$$a_{dd} = \frac{\mu_0 \mu_m^2 m}{12\pi\hbar^2}, \tag{2.2}$$

with the atomic mass m and the reduced Planck constant $\hbar$ and the vacuum magnetic permeability.

2.3. Ultracold quantum gases

The field of ultracold quantum physics is of particular interest because of its broad variety to study quantum phenomena. Both bosonic and fermionic atom gases can be used in the experiments.

Ultracold quantum gases are defined by having atoms at temperatures near absolute zero, which gives rise to quantum phases such as Bose-Einstein condensation, superfluidity, supersolidity as well as droplet, stripe, honeycomb or labyrinth phases to only name a few. All of these states have in common that they show a macroscopic quantum behavior and can be described with Bose or Fermi statistics, depending on their particles spin properties. The observable quantum behavior is due to the large wavelength compared with the usual spacing ($|r_1 - r_2|$) between atoms. The de Broglie wavelength

$$\lambda_{dB} = \sqrt{\frac{2\pi\hbar^2}{m k_B T}} \gtrsim |r_1 - r_2| \tag{2.3}$$

is dependent on the atomic mass m, the reduced Planck constant $\hbar$, the Boltzmann constant k_B and the temperature T. All particles in the condensate are delocalized due to the uncertainty principle

$$\Delta x \Delta y \Delta z \Delta p_x \Delta p_y \Delta p_z = h^3. \tag{2.4}$$

2.3.1. Bose-Einstein-condensate

As predicted by Einstein in 1925 gaseous bosons, i.e. spin-0 particles at low temperatures will condensate to the same quantum state, the Bose-Einstein-condensate (BEC) (after Satyendra Nath Bose and Albert Einstein)[3]. This new state of matter was firstly achieved for dilute atomic gases experimentally in 1995 [1]. The fundamentals of dilute BECs are explained following the derivations of [3] and [1].

When following Boltzmann's classical approach in discretizing the phase space of particles, one can come to the distribution function for bosons (also known as the Bose-Einstein distribution function), which describes the mean occupation numbers for bosons

$$f_{BE}(E) = \frac{1}{e^{\beta(E-\mu)} - 1} \qquad \text{with } \beta = \frac{1}{k_B T}, \tag{2.5}$$

and with E being the energy of the system and μ the chemical potential. Let's consider an ideal three dimensional Bose gas in equilibrium trapped with a 3D harmonic potential (with the trapping frequency ω_i in the three directions $i = x, y, z$). By integrating the Bose-Einstein distribution function the critical temperature T_C is derived (for more detailed information see [3]). If the cloud of non interacting particles is cooled below this critical temperature

$$T_C = \frac{\hbar}{k_B \cdot (\zeta(3))^{1/3}} (\omega_x \omega_y \omega_z \cdot N)^{1/3}, \tag{2.6}$$

where N is the density of the cloud and $\zeta(\alpha) = \sum_{n=1}^{\infty} n^{-\alpha}$ the Riemann zeta function, parts of the gas condense to the BEC. The condensate fraction for this case is

$$N_{tot} = N\Big[1 - \Big(\frac{T}{T_C}\Big)^3\Big]. \tag{2.7}$$

Because particles in the BEC condense to the same state, the gas can be described with a single wave function $\psi(\mathbf{r})$. Applying the mean field approximation the wave function can be described with

$$\psi(\mathbf{r_1}, ..., \mathbf{r_N}) = \prod_{i=1}^{N} \phi(\mathbf{r_i}). \tag{2.8}$$

The wave function is normalized to the total atom number N' in the condensed phase:

$$\int |\psi|^2 d^3\mathbf{r} = N' \tag{2.9}$$

$$\psi(\mathbf{r}) = \sqrt{N'}\phi(\mathbf{r}), \tag{2.10}$$

where $|\psi(\mathbf{r})|^2$ describes the density distribution, i.e. the probability to find a particle at position $\mathbf{r}$.

2.3.2. extended Gross-Pitaevskii equation

In the case of an interacting BEC or more generally ultra-cold quantum gas at finite temperature, one can use the well-established Gross-Pitaevskii equation (GPE) [27] to find the macroscopic wave function:

$$i\hbar\frac{\partial\psi(\mathbf{r},t)}{\partial t} = \Big(-\frac{\hbar^2}{2m}\nabla^2 + V(\mathbf{r}) + \int U_{int}(\mathbf{r}'-\mathbf{r})|\psi(\mathbf{r},t)|^2 \mathrm{d}\mathbf{r}' - \mu\Big)\psi(\mathbf{r},t) \tag{2.11}$$

The equation uses the mean-field approximation for a many-body system of atoms, where their scattering length is much smaller than their interparticle spacing. Since the GPE is a non-linear Schrödinger equation, it cannot be solved analytically.

The first term in Eq.2.11 on the right hand side is the kinetic energy operator $-\frac{\hbar^2}{2m}\nabla^2$. The second term is the potential energy operator of the trap potential. The trap is typically a harmonic trap in three dimensions with the distinct trapping frequencies ω_i:

$$V(\mathbf{r}) = \frac{m}{2}\left(\omega_x^2 x^2 + \omega_y^2 y^2 + \omega_z^2 z^2\right). \tag{2.12}$$

Without more terms this would be the single particle Schrödinger equation without interactions. In the case of a dipolar bosonic quantum gas, the short and long range interactions cannot be neglected. As stated in [28] the general ideal dipole-dipole interaction (DDI) has the following form:

$$V_{dd}(\mathbf{r}) = \frac{C_{dd}}{4\pi}\frac{(\mathbf{e_1}\cdot\mathbf{e_2})r^2 - 3(\mathbf{e_1}\cdot\mathbf{r})(\mathbf{e_2}\cdot\mathbf{r})}{r^5}, \tag{2.13}$$

with $C_{dd} = \mu_0\mu_m$ or d^2/ϵ_0 for the magnetic or electric dipole moments μ_m and d and with $\mathbf{e_{1,2}}$ as the orientation of the dipoles. In the case of strongly interacting polarized dipoles, as prepared in the dysprosium experiment, Eq.2.13 is approximated to

$$V_{dd}(\mathbf{r}) = \frac{C_{dd}}{4\pi}\frac{1-3\cos^2\theta}{r^3}, \tag{2.14}$$

with θ as the angle between the polarization direction. When describing a system, which is governed by short range interactions, the interactions can be approximated to contact scattering with the approximated scattering potential

$$U(\mathbf{r_1}-\mathbf{r_2}) = g_s\delta(\mathbf{r_1}-\mathbf{r_2}). \tag{2.15}$$

where δ is the Dirac-delta-distribution, a_s the s-wave scattering length and $g_s = \frac{4\pi\hbar^2 a_s}{m}$. The third term of the Hamiltonian like function in Eq.2.11 stems from the then used derivation for the combined contact and DDI interactions:

$$U(x_1 - x_2 \equiv \mathbf{r}) = U_s(\mathbf{r}) + V_{dd}(\mathbf{r}) = g_s\delta(\mathbf{r}) + \frac{C_{dd}}{4\pi}\frac{1-3\cos^2\theta}{r^3}, \tag{2.16}$$

with with θ as the angle between the polarization direction and $r = |\mathbf{r}|$. When the average interactions between the atoms become attractive, the mean-field (MF) theory leads to a collapsing dipolar BEC (dBEC) for the many-body ground state (GS), because its density exhibits singularities ($n \to \infty$ so $|E| \to \infty$) [22]. The instability

of the gas arises from the attractive part of the DDI, which in connection with the negative attraction of short range contact interaction averages the MF to zero or less. However, dipolar quantum gases are not collapsing as this theory predicts. Instead they form self bound droplets [29], as well as other exotic phases like supersolids [30], which only collapse in a long-time scale, partly due to three body losses (3BLs) [29]. The stability of dBEC is geometry dependent, with dependence on the trap geometry, the long-range interaction between neighboring clouds, and due to the anisotropy of the dipoles. The additional repulsive contribution stabilizing the system stems from the particles strong dipole interactions, which lead to quantum depletion, meaning corrections of the population as well as corrections to the energy [22]. In 1957, Lee, Huang and Yang calculated the modification of the energy, derived from 2nd order Bogoliubov theory and approximations of the many body Hamiltonian and this correction can be included in the GPE to accurately compute the energy of the dipolar Bose gas [22]. This calculation includes beyond mean field approximations and the so called Lee-Yang-Huang (LHY) correction, which has the following form:

$$\gamma_{QF} = \frac{128\hbar^2}{3m}\sqrt{\pi a_s^5}\,\Re\mathrm{e}(Q_5(\epsilon_{dd})) \tag{2.17}$$

$$\text{with } Q_5(\epsilon_{dd}) = \int_0^1 du(1-\epsilon_{dd}+3u^2\epsilon_{dd})^{5/2} \text{ and } \epsilon_{dd} = \frac{a_{dd}}{a_s}, \tag{2.18}$$

where the auxiliary function $Q_5(\epsilon_{dd})$ can be calculated analytically as demonstrated in [31]. The LHY term includes the effects of quantum fluctuations and the stabilization can also be observed in experiments. ϵ_{dd} is the relative dipole strength to contact interactions and can be positive or negative, for repulsive or attractive interactions, for which in both cases $\gamma_{QF} > 0$ is always true. Including all approximations and corrections, the GPE is then extended to

$$i\hbar\frac{\partial\psi(\mathbf{r},t)}{\partial t} = \underbrace{\left(-\frac{\hbar^2}{2m}\nabla^2 + V(\mathbf{r}) + \int U(\mathbf{r}'-\mathbf{r})|\psi(\mathbf{r},t)|^2\mathrm{d}\mathbf{r}' + \gamma_{QF}|\psi(\mathbf{r},t)|^3\right)}_{\mathcal{L}[\psi]}\psi(\mathbf{r},t). \tag{2.19}$$

In the case of the attractive DDI, the LHY term always stabilizes the system, due to its dependence on $\propto |\psi|^3$ compared to the MF interactions dependent on $\propto |\psi|^2$. When solving the eGPE, the convolution theorem is used to solve the interaction term easily in Fourier space. From now on the Hamiltonian like operator in the eGPE Eq.2.19 will be referred to as $\mathcal{L}[\psi]$. The energy of the system can be found by imposing the stationarity condition $i\hbar\partial_t\psi = 0$. By minimizing the energy, the ground state of the system can be found. This corresponds to solving the eGPE in imaginary time as explained in the next chapter.

2.4. Thomas-Fermi approximation

In the limit of a slow density change of a gas, terms in Eq.2.11 which are proportional to $\hbar$, the kinetic terms, can be neglected [27]. The ground state configuration of the non-dipolar gas then takes a simple form with

$$gn(\mathbf{r}) + V_{trap}(\mathbf{r}) = \mu. \tag{2.20}$$

In the case of a dipolar quantum gas, the interaction between the particles V_{int} needs to be included and the dipolar Thomas-Fermi (TF) approximation is

$$gn(\mathbf{r}) + V_{trap} + V_{DDI} = \mu. \tag{2.21}$$

In this approximation, the density is approximated by a three dimensional parabola. Further explanations can be found in Chap.4 and well as in [32]. The approximation is only valid where the density is far from zero, i.e. the TF approximation breaks down near the edges of the gas.

2.5. Exotic phases in dipolar quantum gases

The magnetic Ln are of interest for their exotic phases among other phenomena. These equilibrium phases with macroscopic textures can be formed because of the long range magnetic dipole interaction [25]. In addition to the pattern formation in Ln, patterns can occur in diverse quantum systems, e.g. superfluid helium, white dwarfs and more ([25]). Important in this thesis for the dysprosium experiment are two different phases: Firstly the superfluid phase, where all particles are condensed in a BEC. Secondly the supersolid phase, where the gas exhibits global superfluid properties as well as being modulated in a crystalline phase. This crystalline phase is characterized by periodic These new phases have a rather stable nature because of their repulsive quantum fluctuations [25]. One parameter of the transition can be the scattering length a_s falling below a critical transition scattering length $a_s < a_s^c$.

2.5.1. Phase transitions

An interesting distinction between phase transitions is whether they are continuous or discontinuous. To quantitatively describe the phase transitions, Lev Landau introduced the now called Landau theory, where an appropriate order parameter ξ is chosen and then analyzed with respect to the free energy as well as its derivatives. Generally known as phase transition of order n, only the distinction between phase transitions of order 1 and 2 is made in this thesis and therefore explained. Following the derivations of [33], [34] and [35], this section explains the fundamental principles about phase transitions, but leaves out everything irrelevant for this specific setting.

2.5.1.1. Order of the phase transition

1st and 2nd phase transitions are classified by their order parameter $\xi(k)$. When crossing the discontinuous (continuous) phase transition at the critical point k_c (of-

ten this is the critical temperature T_c), the order parameter can (cannot) have a finite jump at the transition k_c:

$$\xi(k) = \begin{cases} \text{continuous,} & \text{1st order transition} \\ \text{discontinuous} & \text{2nd order transition.} \end{cases} \tag{2.22}$$

The order parameter is defined by being different on either side of the transition. The Landau free energy for a simple system is

$$\mathcal{F}(\xi) = F_0(k) + V\left(\alpha(k-k_c)\xi^2 + \beta\xi^4 - h\xi\right), \tag{2.23}$$

with the h as an external field, and V as the volume. The parameters α and β define the phase transition. In the case of a system with a global phase symmetry

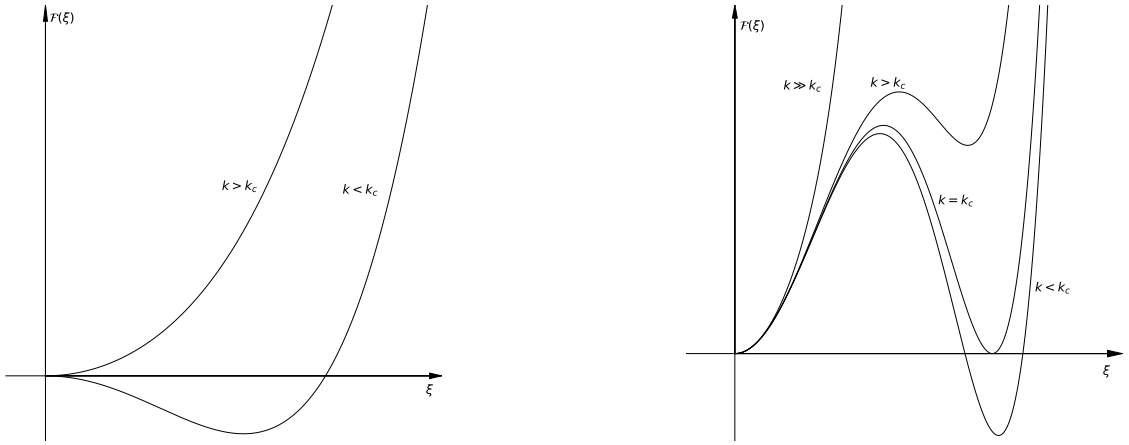

(a) (b)

Figure 2.1.: Qualitative plot for one dimensional free energy. (a) continuous 2nd order phase transition, (b) discontinuous 1st order phase transition.

for $\xi \to \xi e^{i\theta}$, where the angle θ corresponds to the symmetry, the free energy of a BEC can be expanded as

$$\mathcal{F}[\psi^*, \psi] = \int d\mathbf{x}\left[\frac{\hbar^2}{2m}|\nabla\phi(\mathbf{x})|^2 + (V_{ext}(\mathbf{x}) - \mu)|\psi(\mathbf{x})|^2 + \frac{g}{2}|\psi(\mathbf{x})|^4\right]. \tag{2.24}$$

With V_{ext}, μ and g from Sec.2.3.2. This type of potential is called a Goldstone or sombrero potential, see Fig 2.2. For the continuous phase transition, the minima of the free energy can be either one global minimum (above the transition) or an infinite set of minima with all of them being differentiated by a global phase (below the transition), also called the sombrero potential. The two dimensional version is shown in Fig.2.1a. The difference between the cases above and below the transition is dependent on the quadratic coefficient α changing its sign ($\alpha(k = k_c) = 0$). When observing a 2nd order phase transition, the curve expected for $\xi(k)$ is

$$\xi(k) = \sqrt{-\frac{\alpha(k)}{\beta(k)}}, \tag{2.25}$$

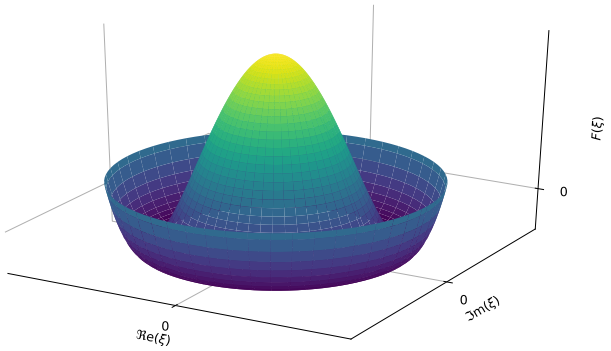

Figure 2.2.: Qualitative Goldstone potential for a system with a phase symmetry of $\xi e^{i\theta}$.

resulting in $\xi(k_c) = 0$. β can generally be dependent on k as well, and give rise to the nature of the transition, but here only the first case is explained.

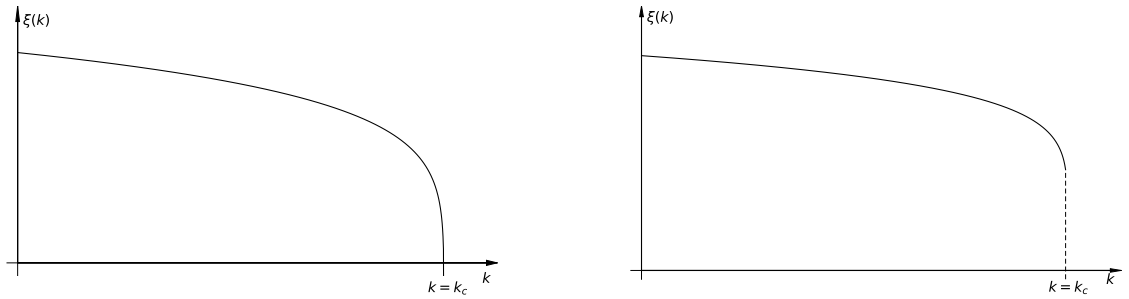

(a) (b)

Figure 2.3.: Qualitative plot for the order parameter ξ. (a) continuous 2nd order phase transition, (b) discontinuous 1st order phase transition.

In the case of a discontinuous phase transition, the free energy will form a second local minimum (belonging to the ordered phase) in addition to the minimum at $\xi = 0$, even before the system undergoes its phase transition. For this case, the free energy will have a term proportional to ξ^6. For $k < k_c$, the free energy is defined by having $\mathcal{F}(k < k_c) < 0$ for certain ξ values, and therefore the order parameter will have a discontinuity at $k = k_c$. The general qualitative graphs are shown in Fig.2.1b and 2.3b for the one dimensional case. Analyzing the order parameter can give insight to the order of the phase transition. In this simulation the order parameter chosen is the density contrast $\mathcal{C}$ dependent on the scattering length a_s. Further explanations follow in Chap.4.

3. Numerical methods

In the following chapter the numerical methods are explained. Firstly the unit system used, then the method of imaginary time propagation to find the ground state of a quantum system, thirdly the split-step-Fourier method, where the time dependent Schrödinger equation is solved by splitting the equation in parts of the momentum and position operator. The goal of the simulation is solving the eGPE (Eq.2.19).

To have calculations with appropriate units, the energy is calculated in units of $\hbar\omega_0$, with $\omega_0^{^{164}\mathrm{Dy}} = 2\pi \cdot 61.63158647\mathrm{Hz}$, which is the appropriate frequency to have $l_0 = \sqrt{\frac{\hbar}{m\omega_0}}$, with the (dysprosium) mass m, the harmonic oscillator length in μm length scale. For that, the eGPE is divided by $\hbar\omega_0$. The terms of the eGPE transform followingly:

$$i\hbar\frac{\partial\psi}{\partial t} \to \frac{i\hbar}{\hbar\omega_0}\frac{\partial\psi}{\partial t} = i\frac{\partial\psi}{\partial\tilde{t}}$$

$$-\frac{\hbar^2}{2m}\nabla^2 \to -\frac{\hbar^2}{2m\hbar\omega_0} = -l_0^2\nabla^2 = -\tilde{\nabla}^2$$

$$V(\mathbf{r}) \to \frac{1}{\omega_0^2 l_0^2}(\omega_x^2x^2 + \omega_y^2y^2 + \omega_z^2z^2) = \tilde{V}(\mathbf{r})$$

$$g|\psi(\mathbf{r},t)|^2 \to 4\pi a_s l_0^2|\psi(\mathbf{r},t)|^2 = \tilde{g}|\psi(\mathbf{r},t)|^2$$

$$\gamma_{QF}|\psi(\mathbf{r},t)|^3 \to 128 l_0^2\sqrt{\pi a_s^5}\,\Re\mathrm{e}(Q_5(\epsilon_{dd}))|\psi(\mathbf{r},t)|^3 = \tilde{\gamma}_{QF}|\psi(\mathbf{r},t)|^3. \tag{3.1}$$

With this unit transformation all results in spacial units are in μm.

3.1. Imaginary time propagation

When trying to find the ground state of a trapped quantum system, it is useful to use imaginary time propagation i.e. replacing $t \to \tau = it$ [36]. The Schrödinger equation then transforms to

$$H\psi = i\partial_t\psi = i\frac{\partial\tau}{\partial t}\frac{\partial\psi}{\partial\tau} = -\frac{\partial\psi}{\partial\tau} \tag{3.2}$$

with H the Hamiltonian of the system. The state is expressed in the eigenbasis of the system

$$\psi = \sum_{k=0}^{\infty} a_k\phi_k, \tag{3.3}$$

where the eigenstates ϕ_n fulfill the Schrödinger equation

$$H\phi_n = -\frac{\partial \phi_n}{\partial \tau} = E_n \phi_n. \tag{3.4}$$

It becomes clear how when waiting for a sufficiently long time $\Delta\tau$, the time evolution of the state

$$\psi(\tau + \Delta\tau) = a_0\phi_0 \cdot e^{-i\Delta\tau E_0} + \sum_{k=1}^{\infty} a_k\phi_k \cdot e^{-i\Delta\tau E_k} \tag{3.5}$$

almost only contains the ground state i.e. the state with the lowest energy. All excited states with a higher energy decay faster and can therefore be neglected. Where in the real time propagation all states are circulating with different phases, in imaginary time propagation they actually decay. It is important to renormalize ψ after each time step Δt by dividing by the norm N'.

$$N' = \int |\psi|^2 dxdydz \tag{3.6}$$

$$\psi' = \frac{\sqrt{N_{tot}}}{N'}\psi, \tag{3.7}$$

with N_{tot} as the total atom number in the condensate. In the numerical calculation, the integral is calculated with the trapezoidal rule. Renormalizing is only necessary when doing imaginary time propagation.

3.2. Split-step-Fourier method

To numerically solve the time dependent Schrödinger equation

$$i\hbar\frac{\partial \psi(\mathbf{r},t)}{\partial t} = \hat{H}\psi(\mathbf{r},t) = \left[\hat{T} + \hat{V}\right]\psi(\mathbf{r},t), \tag{3.8}$$

the split-step-Fourier method (SSFM) [3] is a well established method for solving in three dimensions. For clarity, $\mathbf{r} = x, y, z$ is used, which in general does not refer to radial symmetry. The Hamiltonian $\hat{H}$ can be split into $\hat{H} = \hat{T}+\hat{V}$, with $\hat{T} \equiv -\frac{\hbar^2}{2m}\nabla^2$ the kinetic part and $\hat{V} \equiv V(\mathbf{r},t)$ the potential part of the Hamiltonian, where the kinetic part is local in momentum space and the potential part is local in the real space. The time dependent equation is solved by applying the operator $\hat{H}$ with a small time step Δt to the state before this time step. This is realized as

$$\psi(\mathbf{r}, t + \Delta t) = e^{-i\Delta t\left(\hat{T}+\hat{V}\right)}\psi(\mathbf{r},t). \tag{3.9}$$

$\hat{T}$ and $\hat{V}$ generally do not commute, but Eq.3.9 can be approximated to

$$e^{-i\Delta t\left(\hat{T}+\hat{V}\right)} = e^{-i\Delta t\frac{\hat{T}}{2}}e^{-i\Delta t\hat{V}}e^{-i\Delta t\frac{\hat{T}}{2}} + \mathcal{O}(\Delta t^2). \tag{3.10}$$

Because of the internal interaction term of the eGPE, the order of accuracy drops to $\mathcal{O}(\Delta t^2)$ as stated in [37].

To actually solve the GPE numerically, Eq. 3.9 is transformed to and back from the Fourier space, so the time evolution with small time steps Δt can be written as

$$\psi(\mathbf{r}, t+\Delta t) = \mathcal{F}^{-1}\left[e^{-\frac{i}{2}\Delta t\hat{T}}\mathcal{F}\left[e^{-i\Delta t\hat{V}}\mathcal{F}^{-1}\left[e^{-\frac{i}{2}\Delta t\hat{T}}\mathcal{F}\left[\psi(\mathbf{r},t)\right]\right]\right]\right]. \tag{3.11}$$

While ref. [3] suggests executing $\hat{T}$ once and $\hat{V}$ twice, ref. [37] uses the order of operations as in Eq.3.11. The only difference lies in the duration it takes for the operation to be carried out. Doing the calculations in the reciprocal space generally takes longer because of the need to execute the Fourier transformation (in this case the ψ states are stored in the real space). Eq.3.10 suggests to use the approach of [3] but since the dipole-dipole interaction cut-off (explained further in Sec.3.3.3) also needs a transformation, which takes longer than executing $\hat{T}$ twice, the approach of Eq.3.11 is used.

3.3. Minimization of the energy

To find the ground states of the system, the energy needs to be minimized. The method which is used for the calculation is the split-step-Fourier method as explained in the section above. Now derived are the energy operators $\hat{T}$ and $\hat{V}$.

3.3.1. Kinetic energy

The kinetic energy of the wave function $\psi(\mathbf{r})$ is defined as

$$E_{kin} = -\int d^3\mathbf{r}\psi^*(\mathbf{r})\tilde{\nabla}\psi(\mathbf{r}) = \int d^3\mathbf{r}|\tilde{\nabla}\psi(\mathbf{r})|^2, \tag{3.12}$$

with $\tilde{\nabla} = -l_0\nabla$. To avoid further confusion with the Fourier transformation, from now on $-l_0\nabla = \tilde{\nabla} \equiv \nabla$. The kinetic energy is calculated in Fourier space, by using the transformation

$$\psi(\mathbf{r}) = \frac{1}{(2\pi)^3}\int d^3\mathbf{k}e^{i\mathbf{k}\cdot\mathbf{r}}\tilde{\psi}(\mathbf{k}). \tag{3.13}$$

By taking the gradient and the modulus squared of this expression,

$$\nabla\psi(\mathbf{r}) = \frac{1}{(2\pi)^3}\int d^3\mathbf{k}\nabla e^{i\mathbf{k}\cdot\mathbf{r}}\tilde{\psi}(\mathbf{k}) = \frac{1}{(2\pi)^2}\int d^3\mathbf{k}i\cdot\mathbf{k}\cdot e^{i\mathbf{k}\cdot\mathbf{r}}\tilde{\psi}(\mathbf{k}) \tag{3.14}$$

$$|\nabla\psi(\mathbf{r})|^2 = \left(\frac{1}{(2\pi)^3}\int d^3\mathbf{k}i\cdot\mathbf{k}\cdot e^{i\mathbf{k}\mathbf{r}}\tilde{\psi}(\mathbf{k})\right)^*\left(\frac{1}{(2\pi)^3}\int d^3\mathbf{k}'i\cdot\mathbf{k}'\cdot e^{i\mathbf{k}'\mathbf{r}}\tilde{\psi}(\mathbf{k}')\right) \tag{3.15}$$

$$= \int\frac{d^3\mathbf{k}}{(2\pi)^3}\int\frac{d^3\mathbf{k}'}{(2\pi)^3}\tilde{\psi}(\mathbf{k})\tilde{\psi}^*(\mathbf{k}')e^{i\mathbf{k}\cdot\mathbf{r}}e^{-i\mathbf{k}\cdot\mathbf{r}}\mathbf{k}\cdot\mathbf{k}', \tag{3.16}$$

and then inserting this into Eq.3.19 and integrating over $\mathbf{r}$, the final result for the kinetic energy can be derived as

$$E_{kin} = \frac{1}{(2\pi)^3} \int\int d^3\mathbf{k} d^3\mathbf{k}' \delta(\mathbf{k}-\mathbf{k}') \tilde{\psi}(\mathbf{k}) \tilde{\psi}^*(\mathbf{k}') \mathbf{k}\cdot\mathbf{k}' \tag{3.17}$$

$$= \frac{1}{(2\pi)^3} \int d^3\mathbf{k} |\tilde{\psi}(\mathbf{k})|^2 |\mathbf{k}|^2. \tag{3.18}$$

Evaluating Eq.3.18 leads to a Fourier transformation and an integration instead of a differentiation. Also, this leads to the construction of the kinetic energy operator used in the split step Fourier method. The operator is defined as

$$\hat{T}\psi = -\nabla^2\psi = \mathcal{F}^{-1}\left[k^2 \mathcal{F}\left[\psi\right]\right], \tag{3.19}$$

with $k^2 = |\mathbf{k}|^2$.

3.3.2. Potential energy

The potential energy is a combination of the remaining terms from the eGPE (trapping potential, contact interaction and DDI and the LHY term), but the challenge is to calculate the DDI.

3.3.2.1. Direct dipole-dipole interaction

To successfully solve the eGPE for the system, the effective DDI potential

$$\phi^{DDI}(\mathbf{r}) = \int d^3\mathbf{r}' V_{dd}(\mathbf{r}-\mathbf{r}') n(\mathbf{r}') \tag{3.20}$$

needs to be calculated efficiently. The interaction potential V_{dd} from Eq.2.14 $V_{dd}(\mathbf{r}) = \frac{C_{dd}}{4\pi}\frac{1-3\cos^2\theta}{r^3}$ with θ as the polarization angle and r as the distance between interacting atoms has a divergence at the origin, but by simple Fourier transformations, this numerical challenge is fixed. Eq.3.20, is transformed by applying the convolution theorem ($\mathcal{F}(f*g) = \mathcal{F}(f)\cdot\mathcal{F}(g)$) and which then is derived as

$$\phi^{DDI}(\mathbf{r}) = \int d^3\mathbf{k} e^{i\mathbf{k}\cdot\mathbf{r}} \tilde{V}(\mathbf{k}) \tilde{n}(\mathbf{k}), \tag{3.21}$$

with

$$\tilde{n}(\mathbf{k}) \equiv \int d^3\mathbf{r} e^{-i\mathbf{k}\cdot\mathbf{r}} n(\mathbf{r}). \tag{3.22}$$

and

$$\tilde{V}_{dd} = \frac{C_{dd}}{3}(3\cos^2\alpha - 1) \tag{3.23}$$

and with α the angle between $\mathbf{k}$ and the polarization axis z.

3.3.3. Cut-off potential

The eGPE is solved in both real and Fourier space. In the simulation a discrete Fourier transformation on a finite grid is used and therefore copies of the system

are created. Because of the long range dipole-dipole interaction ($\sim 1/r^3$ compared to exclusively vdW interaction with $\sim 1/r^6$), the DDI potential has to be cut-off. The shape of the cut-off potential is dependent on the characteristics of the trapping potential and one can decide between a semi-analytical cylindrical and an analytical spherical cut-off. The implemented cut-off is based on [28]. The trapping potential used in this simulation is neither cigar nor pancake shaped (which would be characterized by either confined trapping in two directions and loose in one or vise versa), but nevertheless the cylindrical cut-off is used, with

$$U_{dd}^{zyl.cut-off}(\mathbf{r}) = \begin{cases} \frac{C_{dd}}{4\pi}\frac{1-3\cos^2\theta}{r^3}, & |z| < Z_C \text{ and } \rho < \rho_C \\ 0, & \text{otherwise} \end{cases}, \tag{3.24}$$

where ρ (ρ_C) refers to the cylindrical radius (cut-off radius) and z (Z_C) to the height of the cylinder (cut-off height). The Fourier transformation of this is semi-analytic with J_0 the Bessel function of order 0.

$$\begin{aligned} \tilde{U}_{dd}(\mathbf{k}) =& \frac{C_{dd}}{3}(3\cos^2\alpha - 1) \\ &+ C_{dd}e^{-Z_C k_\rho}\Big(\sin^2\alpha\cos(Z_C k_z) - \sin\alpha\cos\alpha\sin(Z_C k_z)\Big) \\ &- C_{dd}\int_{R_C}^{\infty}\rho\, d\rho\int_0^{Z_C} dz\, \cos(k_z z)\frac{\rho^2 - 2z^2}{(\rho^2+z^2)^{5/2}}J_0(k_\rho\rho) \end{aligned} \tag{3.25}$$

The first two terms in Eq.3.25 cut the cylinder off at the top and bottom, the third line is relevant for the lateral wall cut-off. This transformation only needs to be done once, but because of its comparably long calculation time which adds to the calculation time of the direct DDI (Eq.3.20), the order of operation in 3.11 is adapted nevertheless.

3.4. Convergence testing

To judge whether or not the simulation found the ground state within a confidence interval, several different methods can be used. In this thesis the residual res is calculated each 1000th time step in the SSFM

$$res = \frac{\int dxdydz|\mathcal{L}[\psi]\psi - \mu\psi|}{\int dxdydz|\mu\psi|}. \tag{3.26}$$

When the simulation reaches the GS, $res = 0$ because of the condition for the stationary state $\mu\psi = \mathcal{L}[\psi]\psi$. If the simulation is close to the ground state, $-\log_{10} res$ gives an estimate of how close. Furthermore the flatness of this curve is an important indicator to observe. When the simulation is still changing significantly, the residual curve has a gradient close to zero. When ultimately deciding, if the simulation is converged, it is also important to observe the energy, as it should be minimal.

This method only applies to imaginary time simulations.

4. Ground state simulations

The goal is to find the ground states of the BEC-supersolid phase transition, using the imaginary time propagation and with the experimental parameters of the total atom number N_{tot} and the trapping frequencies ω_i, which were measured in the dysprosium experiment. The trapping frequencies ω_i create an asymmetrical trap

N'	$\omega_x[2\pi\text{Hz}]$	$\omega_y[2\pi\text{Hz}]$	$\omega_z[2\pi\text{Hz}]$
$1.24(12)\cdot 10^5$	44.97(12)	10.4(2)	126.3(5)

Table 4.1.: Experimental parameters used in the simulation to find the GS with imaginary time propagation.

for the dipoles. In the simulation two different initial state were used. In the first simulation, the initial state prepared is a Gaussian with noise added on top:

$$\psi = e^{-\left(\frac{\tilde{x}^2}{R_x^2}+\frac{\tilde{y}^2}{R_y^2}+\frac{\tilde{z}^2}{R_z^2}\right)} + noise. \tag{4.1}$$

Here $\tilde{x}_i = x_i - \frac{1}{2}L_i$ (L_i the length scale in μm in direction $i = x, y, z$ in units of l_0) and $R_i = 8 \cdot \sqrt{\frac{\omega_0}{\omega_i}}$. The noise is added by choosing a random matrix $\mathbf{r}$ with the size of the system in all three directions from a Gaussian distribution with $\mu = 0$ and $\sigma = 1$. This matrix $\mathbf{r}$ is then multiplied with a random complex number $e^{2\pi i\theta}$ (θ is a random number between 0 and 1). The amplitude of the noise is chosen by p, in this simulation $p = 0.04$.

$$noise = p \cdot \mathbf{r} \cdot e^{2\pi i\theta} \tag{4.2}$$

Noise is added to break the symmetry of the initial state, so that if the given parameters would result in a non-symmetric state, the simulation will not be stuck.

In a second simulation, a different initial state was used to prevent the bias induced by the Gaussian initial guess. Instead, the initial state prepared is a state only with random noise as in Eq.4.2. This makes sure that no biased outcome is achieved.

4.1. Size of the simulated volume and grid

The condensate is simulated on a finite grid in three dimensions $[\mathcal{N}_{g,x}, \mathcal{N}_{g,y}, \mathcal{N}_{g,z}]$ with the finite lengths L_x, L_y, L_z. To successfully simulate the ground states, the right finite volume and according number of voxels for the simulation needs to be found. A pre-simulation is started with several different dimensional sizes in L_x, L_y, L_z and two different grid sizes [128,256,128] and $[256, 512, 256]$. The energies of the final states with $a_s = 86a_0$ below and $a_s = 92a_0$ above the transition are then compared. The dimensions L_x, L_y, L_z are chosen freely with the condition, that the L_y direction is always the largest one and if $L_x \neq L_z$, then $L_x < L_z$ (because of the trapping

frequency characteristics). Furthermore, the sizes are chosen, so that the total volume ($V = L_x L_y L_z$) is approximately evenly spaced over $V \in [0, 4] \times 10^5 \mu\text{m}^3$. For a larger size of the system, the number of voxels needs to increase accordingly. Therefore, the three dimensional grids of $[128, 256, 128]$ and $[256, 512, 256]$ are used for smaller and bigger system sizes and chosen based on their graphical outcome, meaning that the simulated gas is approximately centered in regarding all three dimensions as well as not having completely saturated 2D pixels, when plotting the 2D densities (see next section on how the simulated gas is plotted). Expected is that once the volume is large enough, the energy for an even larger volume will not change anymore. The simulated gas then is far enough from the edges and the interactions, which are possible in principle due to the calculations in Fourier space, are surpressed. The separation between the outermost interacting particles in two neighboring Fourier copies is smaller than the cut-off radius in that direction. For the states, where both tested grid numbers are working well ($V \leq 81 \times 10^5\,\mu\text{m}^3$), both energies are compared. We can see in Fig.4.1, that with a bigger volume the

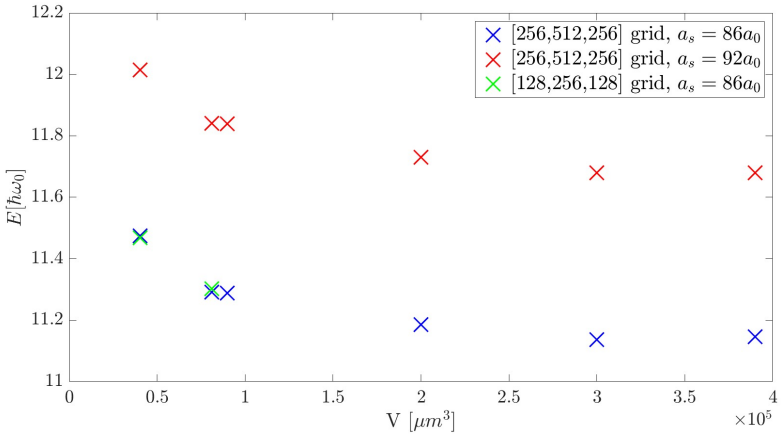

Figure 4.1.: Energy in dependence of simulation volume $V = L_x L_y L_z$. With a larger volume the energy of the final state is closer to the ground state (lower energy). The red and blue points both have the larger $[256, 512, 256]$ grid, whereas the green points use the smaller [128,256,128] grid for the size of the volume, where it is still applicable for comparison. The blue points are calculated for a state below the transition ($a_s = 86a_0$) and the red points are for a state above the transition ($a_s = 92a_0$).

energy decreases down to a certain limit. To make sure that the interplay between having a sufficiently large enough box for the further analysis and a sufficiently small enough box to reduce the calculation time as much as possible, the box size of $L_x = 50l_0, L_y = 120l_0, L_z = 50l_0$ ($V = 3 \times 10^5\,\mu\text{m}^3$) with a $[256, 512, 256]$ grid is used in the following simulations. To confirm that this choice is reasonable, the healing length

$$\xi = \frac{\hbar}{\sqrt{m * \mu}} \tag{4.3}$$

with the dysprosium mass m and the chemical potential μ is calculated and compared with the voxel size dx_i in each dimension x, y, z. For the states below and

above the phase transition with $a_s = 86a_0$ and $a_s = 92a_0$ the condition $\xi > dx_i$ is fulfilled.

4.2. Phase transition

Depending on the scattering length a_s, the condensate is in different phases, namely the isolated droplet (ID) phase, the supersolid (SS) phase and the superfluid (SF) phase. The objective is to identify the phase transition between the supersolid phase and the superfluid phase and to determine whether this transition is continuous or discontinuous. As an order parameter for the Landau theory (see Sec. 2.5.1) the density contrast $\mathcal{C}$ is chosen, because it can characterize the strength of the modulation [30]. The density contrast is calculated in two different ways, further explained Sec.4.2.2.

A challenge of simulating the quantum gas is to accurately simulate the GSs. The goal is to simulate states closest to the GS, which takes longer simulation times to converge as closer a_s is to the phase transition. Whether or not the accurate GS is calculated, also depends on simulation parameters like the box size as explained in the previous section. Depending on the box size, the region of the phase transition can vary as largely as being around $a_s \approx 85.4a_0$ to around $a_s \approx 90a_0$.

As explained before the box size is chosen to be $V = 3 \times 10^5\,\mu\text{m}^3$. The states $a_s \in [86, 92]a_0$ are simulated with $\Delta a_s = 0.5a_0$. The transition is localized within the range of $a_s \in [89, 90]a_0$, so this region is simulated with $\Delta a_s = 0.1a_0$ and then further resolved in $a_s \in [89.9, 89.93]a_0$ with $\Delta a_s = 0.01a_0$.

4.2.1. Qualitative analysis

To qualitatively analyze the phase transition, the calculated GSs in $a_s \in [86, 92]a_0$ are compared based on different criteria: qualitative estimation of the density profile, regarding maxima and minima as well as the number of droplets (distinctly separated density maxima) once they are formed. For the qualitative analysis and especially to identify the number of droplets, the 2D integrated density $n_{x,y}$ is calculated as

$$n_{2D}(x_i, x_j) = \int |\psi|^2 dx_k \quad \text{with } i \neq j \neq k \text{ and } x_i, x_j, x_k = x, y, z. \tag{4.4}$$

The 2D integrated densities along x and y are subject of the qualitative analysis, as in these two directions the gas is modulated eventually, but all three 2D densities are plotted in each first row of the plots in Fig.4.2. The qualitative analysis follows linearly along decreasing a_s for the GS in real space for better clarity. The discussed states can be seen in Fig.4.2.

For $a_s \in [92, 90]a_0$ the quantum gas is in the pure superfluid phase. No density modulations can be observed and the density distribution remains the same for all the simulated states.

For $a_s \in (90, 89]a_0$ the density is modulated in 1 to 4 droplets evenly distributed in a chain. Each time a new density peak is formed, the unmodulated density background is slightly reduced.

For $a_s = 88.5a_0$, the 1D chain of droplets is changed to a 2D crystal, by having a

modulation in the x-direction and forming 7 droplets.
Reducing the scattering length further until $a_s = 86a_0$, the number of droplets rises from 7 to 12, which are further arranged in two dimensions. The minimal density between the peaks is reduced whereas the maximal density rises. It is visible that the transition from the supersolid phase to the superfluid phase is from $a_s = 90a_0$ to $89.9a_0$. Close to the phase SS-SF transition, the density is only modulated close to the trap center, similar to roton trapping [38]. Furthermore it is noted, that in the density modulated region of $a_s \in [86, 89.9]a_0$ the number of droplets is changing from 1 (for $a_s = 89.9a_0$) to the maximal number of 12 ($a_s = 86a_0$) droplets. The arrangement of the droplets in a crystal in one or two dimensions is further analyzed by calculating the two dimensional Fourier transformation of the 2D integrated density:

$$\tilde{n}(\mathbf{k}) = \int n_{x,y} \cdot e^{-i2\pi(k_x x + k_y y)} dxdy. \tag{4.5}$$

The Fourier transformed density displays clearly how the two dimensional crystal exhibits periodicities in several directions (Fig.4.3). All the states show a separated maximum at $k_x = k_y = 0$. This separation occurs because of the halo, the background superfluid in the different states. The state with $a_s = 89a_0$ the Fourier transformation shows droplets being arranged in a chain by showing a modulated *sinc*, as one would expect. For the state at $a_s = 88.5a_0$, where the 1D chain is only disrupted in one chain link, the Fourier density exhibits the same *sinc*-like outline, but this time in two dimensions. For the state $a_s = 86a_0$, which is modulated as a two dimensional hexagonal crystal, the $\tilde{n}_{xy}$ shows the periodic modulations in two diagonal directions and one transversal also in the *sinc* pattern.

To gain a first insight into the phase transition regarding continuity or discontinuity, the calculated density states at $a_s \in [89, 90]a_0$ are compared, with the results regarding the order of the phase transition from the work of [39]. In this work, an infinite dipolar Bose gas is simulated within a cigar shaped trapping potential with confinement in the xy-plane and dipole orientation along the y axis, to understand its phase diagram. With the strong confinement in one direction, the group simulates a reduced 3D system. The wave function is decomposed in the axial and transverse directions $\psi(\mathbf{r}) = \psi(z)\chi(x, y) = \psi(z) \cdot \frac{1}{\sqrt{\pi}l} e^{-(\eta x^2 + \frac{y^2}{\eta})/2l^2}$, where the transverse direction is a Gaussian with variational parameters $\{l, n\}$. The average linear density n along the axial direction. The group finds a direct discontinuous transition from the insulating droplet to the BEC phase for low densities. For intermediate densities, the supersolid phase emerges and the transition between the SS and the BEC is continuous. For high densities, the transition between the SS and the BEC will become discontinuous.

To compare these results with the transition analyzed in this thesis, first, the simulation parameters and physical surroundings have to be compared. As stated, the trap used in [39] is an infinite tube formed trap. In the paper the dipoles are aligned along y, one of the confined directions of the trap. Despite the differences, one can try to compare the present trap to this result to get a first insight into the order of the transition. Because in [39] the supersolid is a one dimensional crystal, the phase transition for the states between the 1D crystal ($a_s \in [89, 90)a_0$) and the superfluid ($a_s \geq 90a_0$) are candidates to compare, by calculating and comparing the

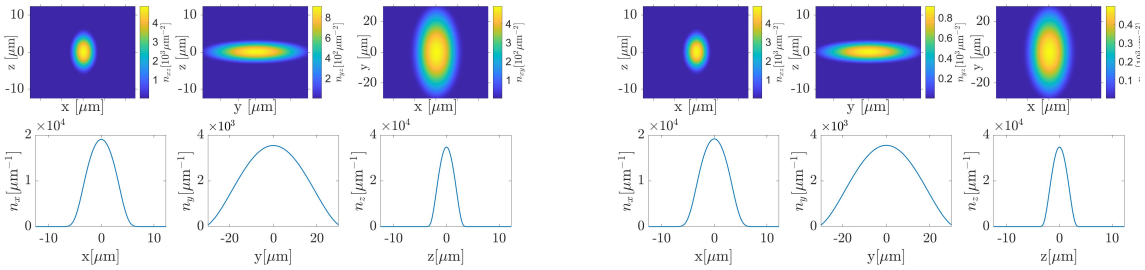

(a) $a_s = 92a_0$

(b) $a_s = 90a_0$

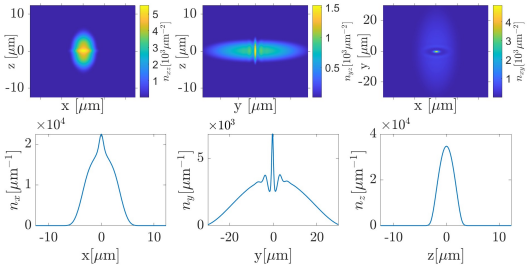

(c) $a_s = 89.9a_0$

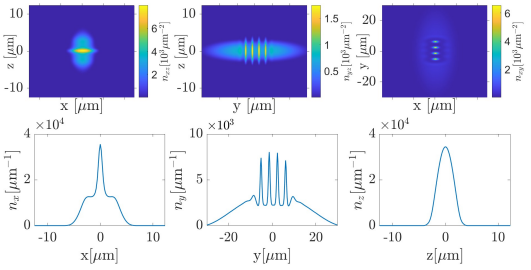

(d) $a_s = 89.5a_0$

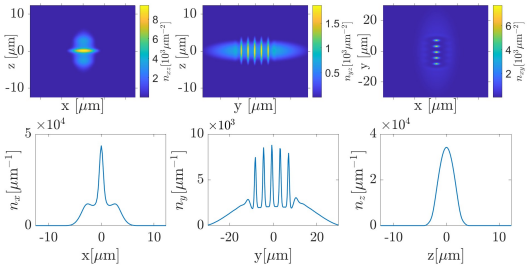

(e) $a_s = 89a_0$

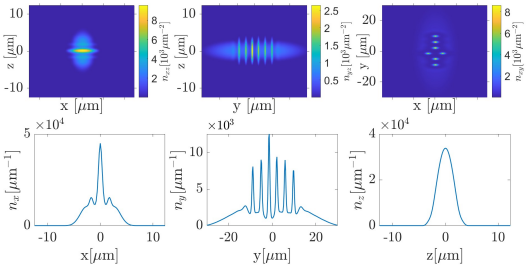

(f) $a_s = 88.5a_0$

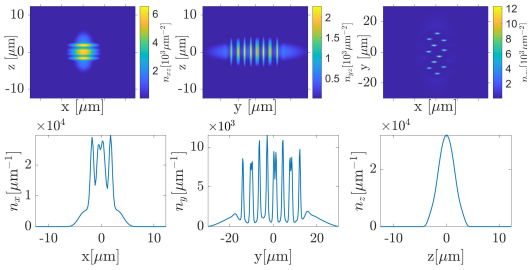

(g) $a_s = 86.5a_0$

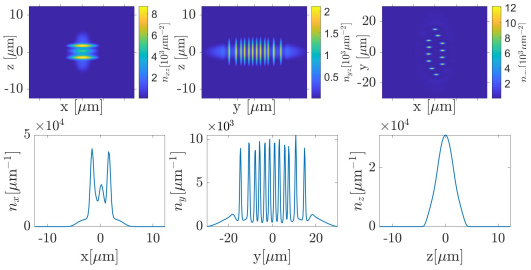

(h) $a_s = 86a_0$

Figure 4.2.: (a)-(h) Simulated ground states for the corresponding scattering length a_s. Simulation with $L_x = 50l_0, L_y = 120l_0, L_z = 50l_0$ and a $[256, 512, 256]$ grid. The SF-SS phase transition is localized in $a_s \in [90, 89.9]a_0$. The plots only show the inner [128,256,128] grid. In the first rows of each Fig.(a)-(h) shows the 2D integrated densities n_{xz}, n_{yz} and n_{xz} from left to right. The colorbar indicates their density. The second rows of each Fig.(a)-(h) show the 1D integrated densities n_x, n_y and n_z from left to right. The other simulation parameters can be found in Tab. 4.1.

1D integrated and averaged densities:

$$n_{1D}(x_i) = \int |\psi|^2 dx_j dx_k \quad \text{with } i \neq j \neq k \text{ and } x_i, x_j, x_k = x, y, z. \tag{4.6}$$

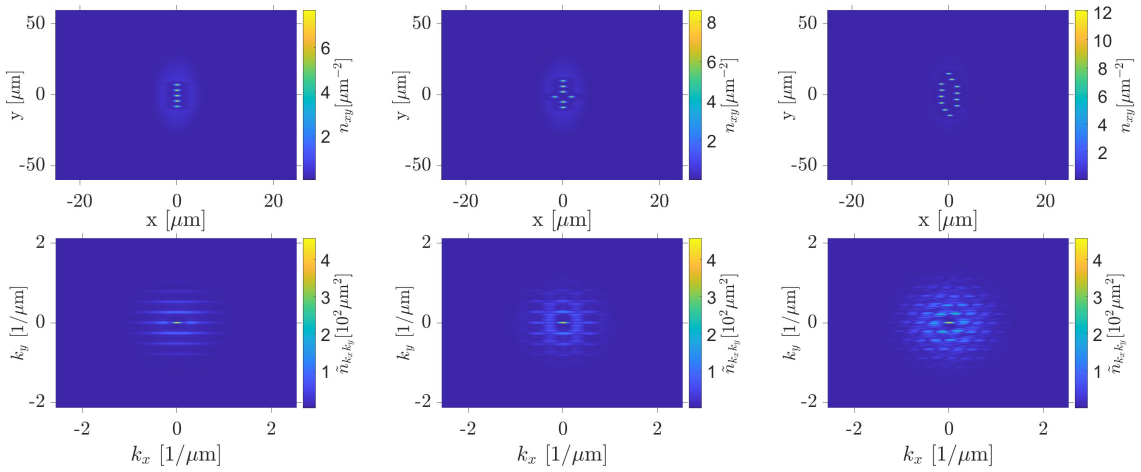

(a) $a_s = 89a_0$ (b) $a_s = 88.5a_0$ (c) $a_s = 86a_0$

Figure 4.3.: Fourier transformed 2D integrated densities for the indicated states. The first row shows the 2D integrated density n_{xy}. The second row shows the according Fourier transformed 2D density $\tilde{n}_{xy}$. The colorbars indicate the densities and Fourier densities.

The 1D integrated densities are plotted in each second row of Fig.4.2a-4.2h. The mean density is then calculated with

$$\langle n_{i,1D} \rangle = \frac{1}{L_i'} \int_{L_j, L_k, L_i'} dx_i dx_j dx_k |\psi|^2, \tag{4.7}$$

L_i' being a reduced length compared to L_i. This is chosen, because of the large box size, the atom cloud is far from the edges. L_i' is chosen by enclosing 99.9% of the total density. For all states in $a_s \in [89, 90)a_0$, the average density is around $\langle n_y \rangle = (2.0 \pm 0.1) \times 10^3\,\mu\text{m}^{-1}$. When comparing this density with Fig.1(a) from [39], the result of the paper is a continuous phase transition, when changing the scattering length a_s from $89a_0$ to $90a_0$. To further analyze the transition, the density contrast is now calculated and analyzed.

4.2.2. Contrast

In the transition region of $a_s \in [86, 92]a_0$, the density contrast $\mathcal{C}$ is measured in two different ways and then compared. The common definition of the density contrast is

$$\mathcal{C} = \frac{|n_{max} - n_{min}|}{n_{max} + n_{min}}, \tag{4.8}$$

which makes the contrast a quantitative variable to compare different strengths of density modulations. The density n_{max} and n_{min} can be the densities in one to three dimensions. However, for a first result, $\mathcal{C}$ is measured analogue to [40], where the density contrast is measured differently to Eq.4.8. In this approach, one dimensional density modulations are measured. Here, the y direction is identified as the direction where the prominent modulation takes place, eventhough the x

direction also exhibits some modulation, only the y direction is analyzed. In both methods, for $\mathcal{C} = 0$, the ground state exhibits no modulations and is identical to the ψ_{BEC} ground state.

4.2.2.1. Method 1

The contrast $\mathcal{C}_1$ is measured in the following way: First the 1D integrated density is calculated (Eq.4.6), where then the modulation region boundaries are identified. This is done automatically by ensuring that the region encloses $p\%$ of the total density

$$n'_y = p\% \cdot n_{y,tot} \tag{4.9}$$

For the sake of simplicity, the boundaries are chosen symmetrically around $y = 0$,

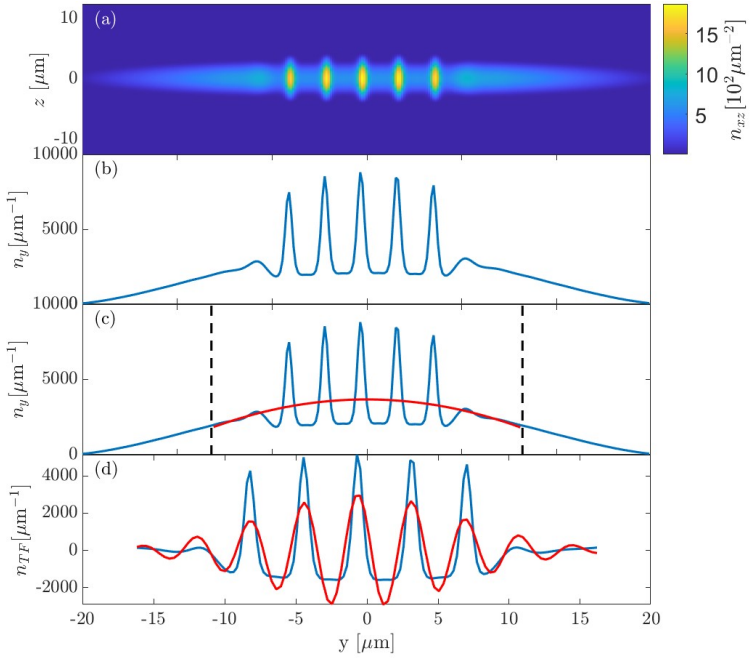

Figure 4.4.: Contrast analysis method with $a_s = 89a_0$. The modulated direction is identified as the y-direction. (a) the 2D integrated density $n_{2D}(y)$, (b) the 1D integrated density $n_{1D}(y)$. (c) 1D integrated density $n_{1D}(y)$ (blue) and Thomas-Fermi fit $n_{1D}^{TF}(y)$ (red) within the boundaries (black dashed lines). (d) Residual density $n_{res} = n_{1D} - n_{1D}^{TF}(y)$ (blue) and fitted function for the residual $n_{1D}^{res}(y)$. This analysis is calculated for all the states $a_s \in [86, 92]a_0$.

eventhough the density curves are generally not. The resulting error is considered negligible. The percentage of the total density is different for different stages of the transition. In a_s ranges with high density contrast (i.e. separated droplets) $p\% = 0.99$, for intermediate contrast $p\% = 0.96$ and for low contrast (condensate) $p\% = 0.4$ to 0.2. For this fitting region with the calculated boundaries (Eq.4.9) a

one dimensional Thomas-Fermi curve is fitted:

$$n_{1D}^{TF}(x_i) = a_1 - b_1(x_i - c_1)^2. \tag{4.10}$$

a_1, b_1 and c_1 are the fitting parameters, which are responsible for the height of the function, the curvature and its horizontal shift. The density residual $n_{res} = n_{1D} - n_{1D}^{TF}$ is calculated and then fitted with

$$n_{1D}^{res} = a_2 \sin(b_2 x_i + c_2) e^{-d_2(x_i - e_2)^2}. \tag{4.11}$$

This is used as a fitting curve, to match the seeming periodical modulation as well as the overall envelope of the curve. Finally the contrast is calculated as the ratio between the residual fit and the Thomas-Fermi fit amplitudes

$$\mathcal{C}_1 = \left|\frac{a_2}{a_1}\right|. \tag{4.12}$$

This way of measuring the contrast, by calculating how much impact the modulation has over the overall density function is in theory a seemingly legitimate way of calculating the contrast. For states, where there is only a bit modulation compared to the overall smooth density, the fitting parameter a_1 will be large compared to the vertical width of the residual fit. For states with a high density modulation, the underlying Thomas-Fermi approximated curve will be small compared to the modulation. For these states with large modulations, it is possible to have a contrast higher than 1. By taking the quotient of these measures, the effects of the modulation are taken into account. This contrast $\mathcal{C}$ is calculated for all states from

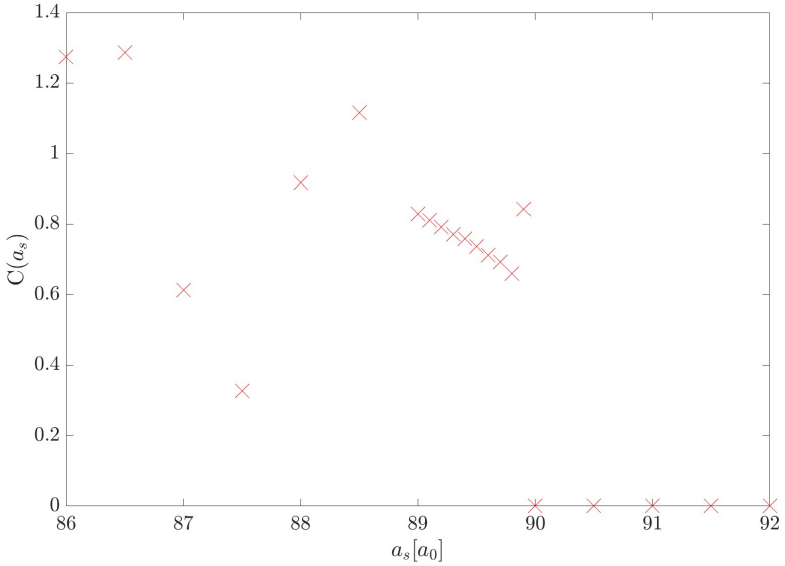

Figure 4.5.: Calculated contrast $\mathcal{C}(a_s)$ for all simulated states $a_s \in [86, 92]a_0$.. The contrast $\mathcal{C}$ is calculated with the fit parameters $\mathcal{C} = |\frac{a_2}{a_1}|$.

$a_s \in [86, 92]a_0$ and then put into a diagram $\mathcal{C}(a_s)$ to see if the curve is continuous or discontinuous. The general method can be seen in Fig.4.4 and the result in Fig.4.5.

The states from $a_s \in [86, 90]a_0$ are all simulated with $\Delta a_s = 0.5a_0$, additionally in the transition region of $a_s \in [89, 90]a_0$, they are simulated with $\Delta a_s = 0.1a_0$ to give more insight into the transition. This way of calculating the contrast only works for a one dimensional modulation. Regardless it is also calculated for the states in $a_s \in [86, 89)a_0$, which are ordered in a 2D crystal. This results in a systematical error, which can clearly be seen in the result. As soon as the modulation is only along the y-direction for $a_s \in [89, 90)a_0$, this method seem to work well. Nevertheless the value of $\mathcal{C}(89.9a_0)$ stands out particularly. The contrast is measured with the amplitude of the fitted function, but the systematical error of insufficient fit leads to changing contrasts. The fit functions for $a_s \in [89, 89, 8]a_0$ underestimate the amplitude as can be seen in Fig.4.6. The best fit result is achieved for $a_s = 89.9a_0$, where as the other results do not seem to be fitted as accurately. This is the reason, why for determining the contrast gap, the contrast value for $a_s = 89.9a_0$ is used and the result is $\Delta\mathcal{C}(89.9a_0) = 0.841$.

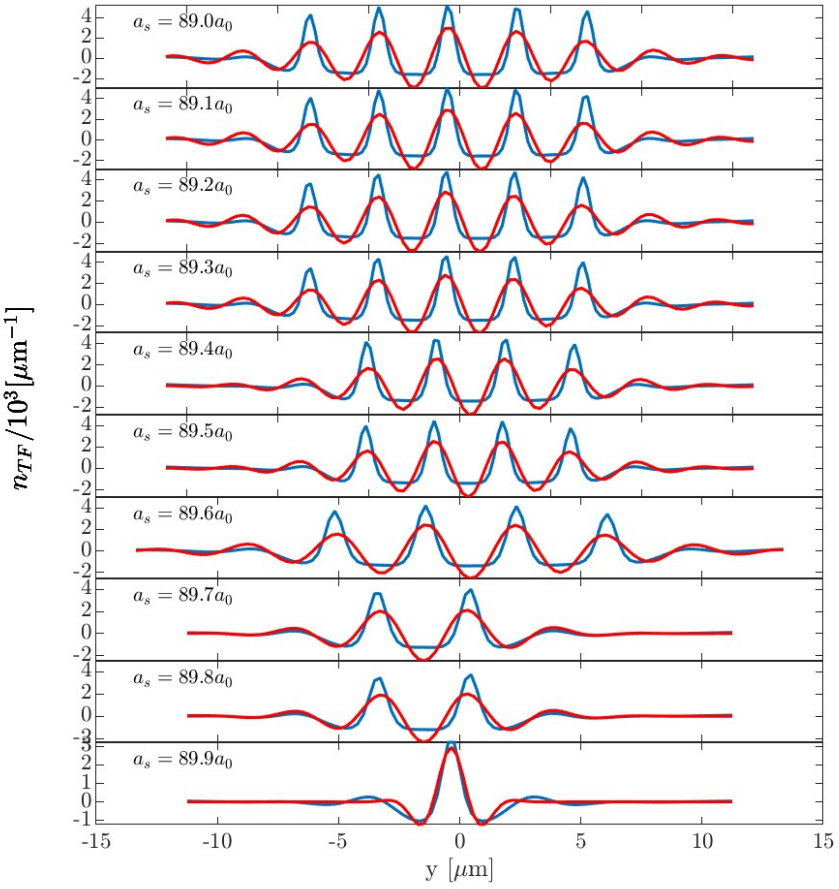

Figure 4.6.: Fitted residual functions $n_{1D}^{res}(y)$ for $a_s \in [89, 89.9]a_0$.

4.2.2.2. Method 2

Because the first method of calculating the contrast $\mathcal{C}A1$ did lead to systematical errors, another way to measure the contrast is used. For this the common definition of the contrast $\mathcal{C}_2$ as in Eq.4.8 is used for the 1D integrated densities as in Eq.4.6. The

maximal and minimal densities however are not the overall maximal and minimal densities in the modulation region, but the ones closest to 0. This is used to account for the fact that the actual 2D modulation from $a_s \in [86, 89)a_0$ leads to overlapping droplets in the 1D integrated density. The maximum, which is taken for n_{max}, is made to be sure to not have overlapping droplets in the 1D integrated density. The minima next to the central peaks are both calculated and the lower one is then used to calculate the contrast. The contrast is computed also for all states in $a_s \in [86, 92]a_0$ and the results can be seen in Fig.4.7. When analyzing both contrasts

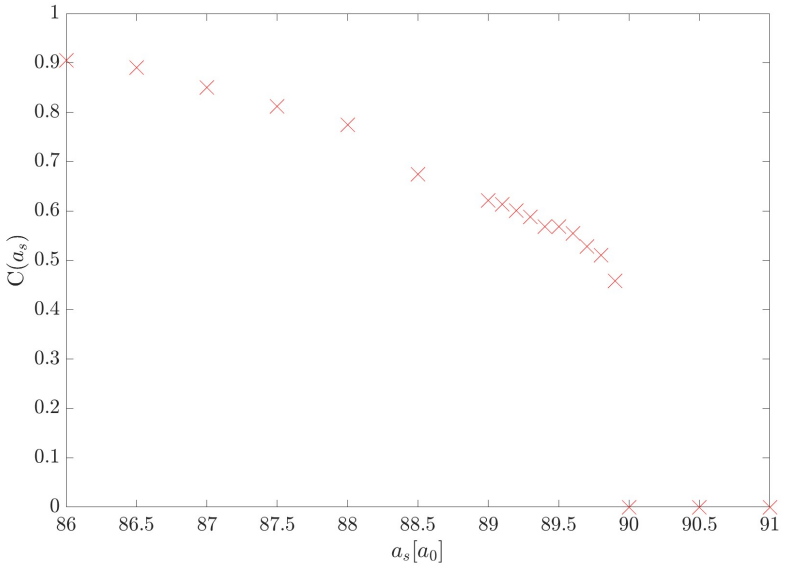

Figure 4.7.: Calculated contrast $\mathcal{C}(a_s)$ for all simulated states $a_s \in [86, 92]a_0$. The contrast $\mathcal{C} = \frac{|n_{max} - n_{min}|}{n_{max} + n_{min}}$ is calculated with the central 1D integrated density maxima and minima in the y-direction for non overlapping droplets.

graphically in Fig.4.5 and Fig.4.7, the finite gap can be identified in $a_s = 89.9a_0 \rightarrow a_s = 90a_0$, with a gap of $\Delta\mathcal{C}_1 = 0.841$ and $\Delta\mathcal{C}_2 = 0.458$.

When comparing the two different methods to measure the contrast, they both have the disadvantage of only being able to treat one dimensional crystals properly. A better way to qualitatively analyze the 2D crystal more could be to calculate the 2D density contrast with Eq.4.8 with two dimensional maxima and minima. However calculating the density contrast with maximal and minimal values of the density in the modulated region close to the center of the trap, worked well and is thus taken as the final result for the finite contrast gap of $\Delta\mathcal{C} = 0.485$.

To determine if the transition is continuous or discontinuous, it is to determine if the order parameter $\mathcal{C}$ has a finite gap comparable to Fig.2.3a. With the geometry chosen the phase transition is found to be discontinuous with a finite contrast gap of $\Delta\mathcal{C} > 0.45$. The system simulated is a finite sized system, which theoretically is expected to have a continuous phase transition, by simulating infinite ground states. To further investigate, more ground states must be resolved.

With the chosen geometry a strong competition between forming a 1D or 2D

crystal is found. The transition between those is dependent on the scattering length too, like the phase SF-SS phase transition. However this needs to be further investigated.

5. Dynamical simulations

The goal in this part is to simulate a dynamical time evolution of the quantum gas, where the scattering length a_s is quenched linearly over time, to observe the phase transition in real time propagation. The observed phase transition is simulated with the same set of a_s values and other parameters as the GS simulations.

5.1. Linear quenching

To observe the transition in the region around $a_s \in [86, 92]a_0$, the initial state with $a_s = 92a_0$ runs first without quenching a_s, then the linear quench is applied, to finally end with constant $a_s = 86a_0$. The quench function for this scenario is

$$a_{s,1}(t)[a_0] = \begin{cases} 92a_0, & \text{for } 0ms < t < 50ms \\ -0.6\frac{a_0}{ms}t[ms] + 122a_0 & \text{for } 50ms < t < 60ms \\ 86a_0 & \text{for } 60ms < t < 100ms \end{cases} . \tag{5.1}$$

The initial state fed into the simulation is chosen to be the ground state for the dynamical simulation at $t = 0$ with $a_s = 92a_0$ calculated in Sec.4.

A second simulation was carried out with the following linear quench, to compare a different final state with the corresponding ground state:

$$a_{s,1}(t)[a_0] = \begin{cases} 92a_0, & \text{for } 0ms < t < 50ms \\ -\frac{1}{3}\frac{a_0}{ms}t[ms] + 107a_0 & \text{for } 50ms < t < 60ms \\ 89a_0 & \text{for } 60ms < t < 200ms \end{cases} . \tag{5.2}$$

5.2. Thermal noise

When investigating the dynamical case, thermal fluctuations must be taken into account. Here, they are approximated by calculating the thermal noise once and then adding it randomly to the simulation. Analogue to [41], but for a three dimensional setting, the fluctuations are calculated as

$$\psi(\mathbf{r}, t = 0) = \alpha \sum_{n,l,m}{}' \phi_n(x)\phi_l(y)\phi_m(z), \tag{5.3}$$

where $\phi_j(i)$ are the eigenmodes of the non-interacting 1D harmonic oscillator. α is a random variable with the mean $\langle|\alpha|^2\rangle = (e^{\frac{(\epsilon_{nlm}-\mu)}{k_bT}} - 1)^{-1} + \frac{1}{2}$, where $\epsilon_{nlm} = \hbar(\omega_x(n + \frac{1}{2}) + \omega_y(l + \frac{1}{2}) + \omega_z(m + \frac{1}{2}))$ is the corresponding eigenenergy. The $\sum'$ indicates that the sum is restricted to $\epsilon_{nlm} < 2k_bT$. In this simulation $T = 50$nK is used as well as the experimental parameters from Tab. 4.1.

5.3. Results

The simulation was firstly carried out with a the first suspected phase transition region covered by $a_s \in [85.3, 86]a_0$ and a $[128, 256, 128]$ grid, with the dimensions of $L_x = 24l_0, L_y = 70l_0$ and $L_z = 30l_0$. This size of the system turned out to be too small of a box (see Fig.5.1). The simulated dysprosium gas reaches very close to the boundaries and is therefore interacting in a non physical way. The result is, that an excited state is simulated instead of covering the ground state phase transition. With the then adapted length scales and box sizes as well as linear quench function

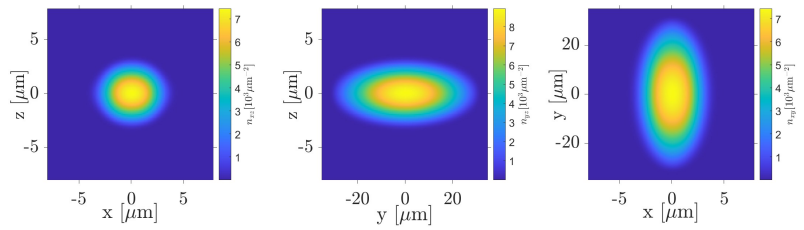

(a) $t = 0$

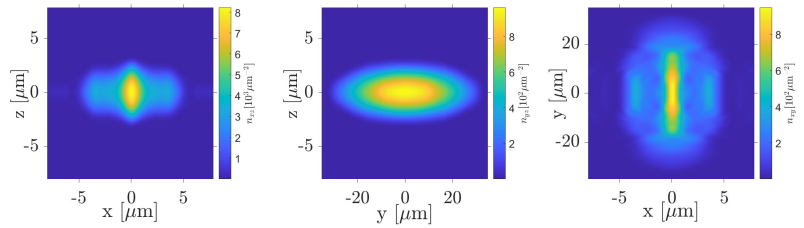

(b) $t = 3.87ms$

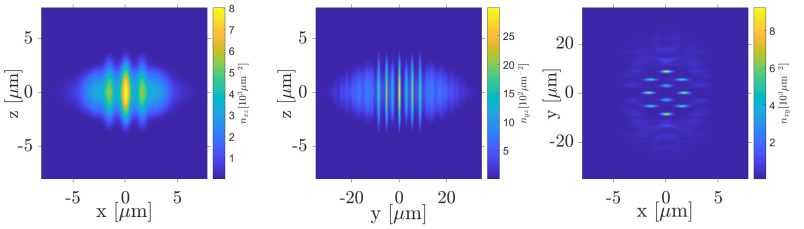

(c) $t = 12.9ms$

Figure 5.1.: First dynamical quench on a [128,256,128] grid with $L_x = 24l_0, L_y = 70l_0$ and $L_z = 30l_0$.

(Eq.5.1), the dynamics are simulated again.

5.4. Analysis

5.4.1. Qualitative analysis

When qualitatively analyzing the simulation, the thermal noise can be observed nicely, as the density distribution has a rough surface. The condensate even seems to be modulated periodically in the density at certain times even before the quench begins, but modulates itself back to the condensate state. For both quenches the final states are different from the calculated corresponding ground states. When

the quench is completed the crystal shows transversal vibrations in the x-direction. When the simulated quantum gas is quenched with the first quench (Eq.5.1, results can be seen in Fig.5.3), the formation of droplets can be seen after a short response time, which will be analyzed further in the next section. Same as in the GS simulations the first number of droplets is 1, however when further quenching, it becomes clear that there is a different number of droplets for the final state, which is between 17 and 19, compared to the ground state simulation for $a_s = 86a_0$ with 12 droplets (see chapter 4).

The second simulation (results in Fig.5.4), which was done with the quench Eq.5.2 also has a different number of droplets for the final state with 3 compared to the GS simulation with 5 droplets for $a_s = 89a_0$. The three droplets are only slightly arranged in a 2D crystal and show the transversal vibrational mode with the greatest amplitude for the middle droplet. The response time for this quench cannot be seen as clearly as for the first quench when analyzing the simulation only qualitatively.

5.4.2. Response time

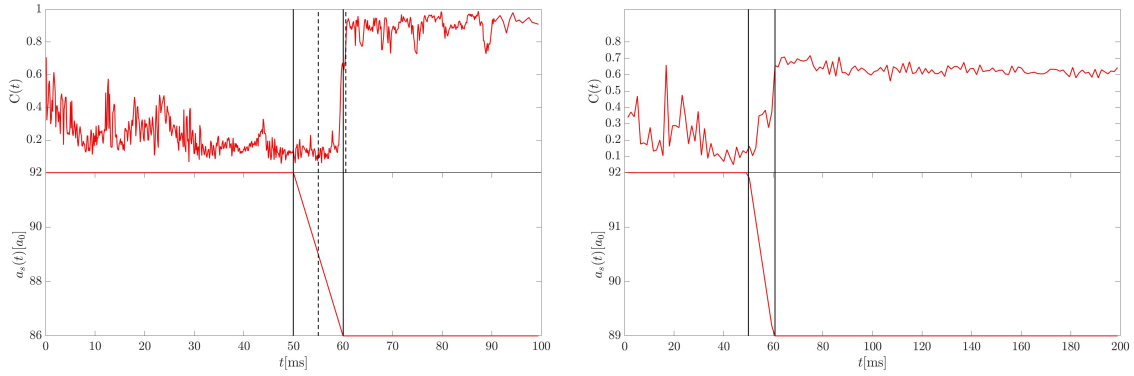

(a) (b)

Figure 5.2.: The contrast $\mathcal{C}(t)$ in direct comparison with $a_s(t)$. The solid black lines indicate the time of the linear quench, the dotted line (if existing) the threshold time t_1 to calculate the response time Δt. (a) Quenching according to Eq.5.1, (b) Quenching according to Eq.5.2.

When doing dynamical simulations, it is interesting to analyze the response time of the system due to the quench. Here it is calculated by calculating the density contrast of the modulation and comparing it with the time t at which the scattering length parameter $a_s(t)$ is expected to transition based on the ground state calculations. The contrast $\mathcal{C}$ is calculated as in the second method in Sec.4.2.2 with the difference of not choosing the maxima and minima closest to 0 but by choosing the highest maximum and its neighboring minimum. For states where the droplets lead to an overlap in the 1D integrated density this method leads to errors, but because of the thermal noise, this is the best way to choose. The response time of the system is defined as the time interval Δt between the time t_1 with $a_s(t_1) = 89.9a_0$ and the time t_2 where $\mathcal{C}(t_2) > 0.75$ for the first quench or $\mathcal{C}(t_2) > 0.5$ for the second quench with $t_1 < t_2$. The thresholds for the two different quenches where chosen

based on the graphical analysis of $\mathcal{C}(t)$. The response time for the quench in Eq.5.1 and Fig.5.3 is $\Delta t = 5.5521ms$. For the quench in Eq.5.2 and Fig.5.4, the response time could not be calculated, because $t_1 = t_2$ were identical. To further analyze the response time for this second quench, a simulation with smaller time steps in the split step Fourier method needs to be carried out.

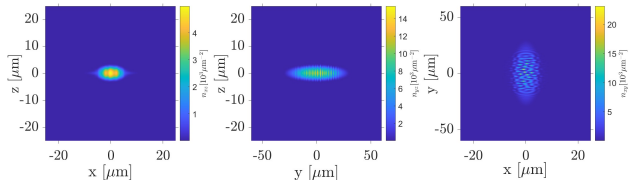

(a) $t = 0.387$ms

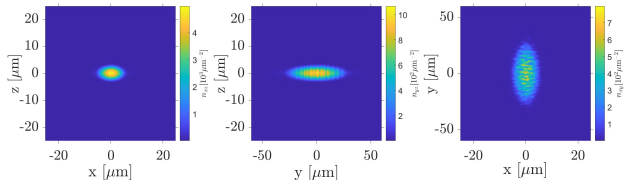

(b) $t = 49.969$ms

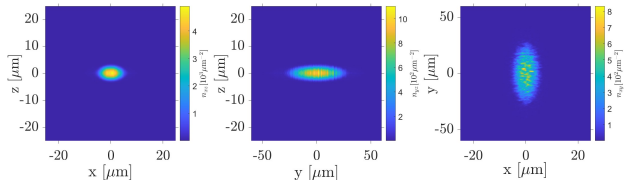

(c) $t = 55.521$ms

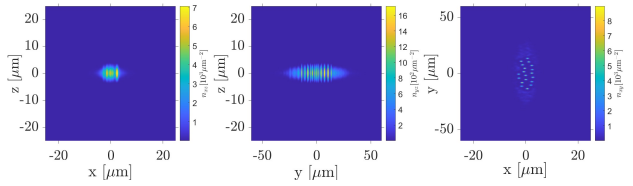

(d) $t = 71.015$ms

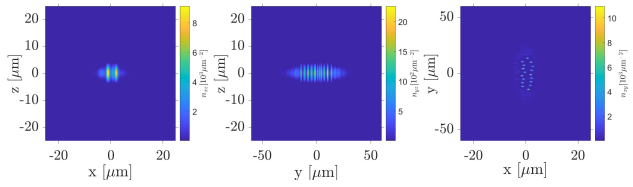

(e) $t = 90.383$ms

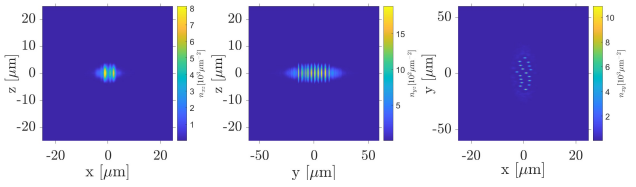

(f) $t = 100.066$ms

Figure 5.3.: Dynamical simulation with 10ms linear quench for $a_s \in [92, 86]$ from $t = 50$ms to $t = 60$ms for $L_x = 50l_0, L_y = 120l_0, L_z = 50l_0$ and a $[256, 512, 256]$ grid at different time t.

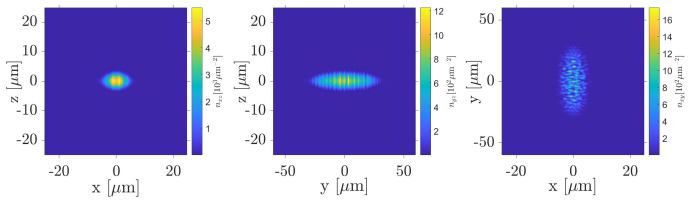

(a) $t = 0$

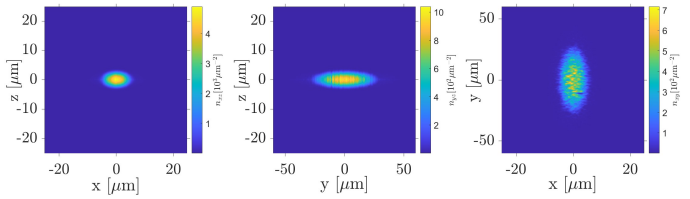

(b) $t = 49.065$ms

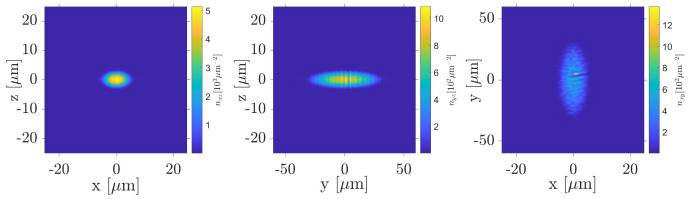

(c) $t = 58.103$ms

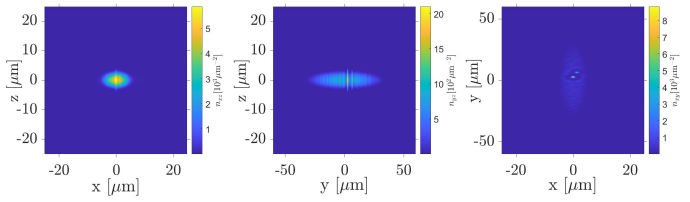

(d) $t = 64.559$ms

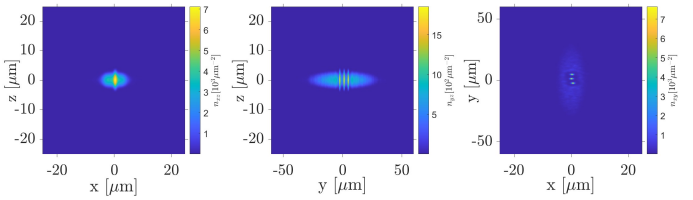

(e) $t = 103.294$ms

Figure 5.4.: Dynamical simulation with 10ms linear quench for $a_s \in [92, 89]$ from $t = 50$ms to $t = 60$ms for $L_x = 50l_0, L_y = 120l_0, L_z = 50l_0$ and a $[256, 512, 256]$ grid at different time t.

When quenching the system from $a_s = 92a_0$ to a scattering length below the superfluid-supersolid transition, the system will eventually undergo the transition. However for both simulated quenches the final state of the system is different from the corresponding calculated ground state. The response time for the eventual transition was calculated for the bigger quench (Eq.5.1) as $\Delta t = 5.5521ms$ and could not be calculated for the second smaller quench (Eq.5.2), presumably due to less data points, but for a definite conclusion the simulation must be repeated with a smaller time step dt in the SSFM and more saved states, to be able to calculate the response time with more accessible data points. Similar to the GS simulations a

strong competition between a 1D and a 2D arranged crystal can be observed. Here the thermal fluctuations enhance the change between the arrangement in one or two dimensions.

6. Conclusion

The objective of this thesis was the theoretical investigation of the phase transition between the superfluid and the supersolid phase in a dysprosium condensate with the experimental parameters of the DyLab.

The transition to the modulated state was identified at $a_s = 89.9a_0$, which supports supersolid characteristics. For scattering lengths $a_s \in [89, 89, 9]a_0$ the modulation was found to be in a one dimensional arrangement with increasing droplet number for decreasing a_s. For $a_s \in [88.5, 86]a_0$ the droplets are arranged in a two dimensional crystal.

The phase transition was first analyzed by calculating the ground states for different scattering lengths $a_s \in [92, 86]a_0$. Closer to the phase transition more states were simulated for smaller scattering lengths gaps to obtain a clearer picture of the phase transition. To investigate the phase transition quantitatively, the density contrast $\mathcal{C}$ was measured in two different ways. The first way relied on the quotient of the modulation amplitude with respect to a fitted Thomas-Fermi approximation to quantize the strength of the density modulation. This method was only applicable to 1D modulated crystals, and even then systematic errors remained in the fit. This method seems to be applicable only for very small density modulations, where almost all particles are condensed. The second method, where the one dimensional density contrast was computed and the maxima and minima of the density were extracted. This method works well for 1D modulated crystals. When the condensate crossed the transition to the two dimensional crystal, this method was still applicable with small adjustments (selecting the central peak and not the largest peak and ruling out maxima, where two droplets overlapped in the 1D integrated density). This approach leads to systematic errors, by not always calculating the largest possible density contrast, but we decided to neglect these errors.

By comparing the results with the Landau theory of phase transitions, the contrast suggests a discontinuous phase transition with a gap of $\Delta\mathcal{C} = 0.458$.

What remains to be investigated is the analysis of ground states even closer to the transition in $a_s \in (89.9, 90)a_0$, as well as for the transition between the 1D chain and the 2D crystal in $a_s \in (88.5, 89)a_0$. For this transition, the two-dimensional density contrast may give insight. Another way to proceed to analyze the superfluid-supersolid transition as well as the transition from the 1D to the 2D crystal, can be to calculate the superfluid fraction to have an additional order parameter analysis for the Landau theory. To fully analyze all aspects of the phase transition between the superfluid and the supersolid phase, the transition must be analyzed with the number of particles as the changing variable to complete a phase transition diagram.

In the second part of the thesis, a real time simulation with a dynamical quench in the scattering length was performed to compare the phase transition and the stated reached dynamically to the before calculated ground states. Two different quenches with were applied in two separate simulations. The first used a quench

from $a_s = 92a_0$ to 86_a0 and the second used a quench from $a_s = 92a_0$ to 89_a0. In the simulation thermal noise was added to account for thermal excitations of the condensate. We observed a dynamical transition to a modulated state, which is delayed compared to expectations from ground state calculations. The response time of the system could only be calculated for the quench with $a_s \in [92, 86]a_0$ and was calculated as $\Delta t = 5.5521$ms. This response time could in further investigations be related to the Kiple-Zurek mechanism, where the correlation time of a system diverges at a phase transition resulting in a delayed response. Analyzing defects in the calculated states could be possibly connected with the diverging correlation length in the Kiple-Zurek mechanism. When comparing the states of the gas after the quench is finished, both quenches settle on different states as the before calculated ground states suggested. To further analyze this difference, more quenches should be simulated. With more identical quenches, the density could be averaged to more conclusively analyze the response time. By simulating different quenches with different quench rates and different relaxation times after the quench. Another aspect which would be interesting to analyze is changing the trap parameters dynamically. This could include a quench from the used anisotropic trap to a cigar shaped trap ($\omega_x = \omega_z$) or even further to a pancake shaped trap ($\omega_x = \omega_y$). Future works might investigate the dependence of the final state on these parameters.

A. Appendix

List of Figures

Bibliography

[1] C. J. Pethick and H. Smith. *Bose-Einstein Condensation in Dilute Gases*. Cambridge University Press, 2001.

[2] N. P. O. AB. *Press Release*. `https://www.nobelprize.org/prizes/physics/2001/press-release/`. Accessed: 2024-06-11. 2024.

[3] C. Barenghi and N. G. Parker. *A Primer on Quantum Fluids*. Springer International Publishing, 2016.

[4] J. Allen and A. Misener. "Flow of Liquid Helium II". In: *Nature* 141 (1938), p. 75.

[5] P. Kapitza. "Viscosity of Liquid Helium below the -Point". In: *Nature* 141 (1938), p. 74.

[6] F. London. "The -Phenomenon of Liquid Helium and the Bose-Einstein Degeneracy". In: *Nature* 141 (1938), pp. 643–644.

[7] F. London. "On the Bose-Einstein Condensation". In: *Phys. Rev.* 54 (11 1938), pp. 947–954.

[8] L. Tisza. "Transport Phenomena in Helium II". In: *Nature* 141 (1938), p. 913.

[9] L. Landau. "Theory of the Superfluidity of Helium II". In: *Phys. Rev.* 60 (4 1941), pp. 356–358.

[10] N. BOGOLUBOV. "T4 - ON THE THEORY OF SUPERFLUIDITY**J. Phys. (USSR) 11, 23 (1947)." In: *Helium 4*. Ed. by Z. M. GALASIEWICZ. Pergamon, 1971, pp. 247–267.

[11] J. Léonard et al. "Supersolid formation in a quantum gas breaking a continuous translational symmetry". In: *Nature* 543.7643 (Mar. 2017), 87–90.

[12] T. Donner. "Dipolar Quantum Gases go Supersolid". In: *Physics* 12 (2019), p. 38.

[13] G. V. Chester. "Speculations on Bose-Einstein Condensation and Quantum Crystals". In: *Phys. Rev. A* 2 (1 1970), pp. 256–258.

[14] A. F. Andreev and I. M. Lifshitz. "Quantum Theory of Defects in Crystals". In: *Soviet Physics Uspekhi* 13.5 (1971), p. 670.

[15] A. J. Leggett. "Can a Solid Be "Superfluid"?" In: *Phys. Rev. Lett.* 25 (22 1970), pp. 1543–1546.

[16] S. Balibar. "The enigma of supersolidity". In: 464.7286 (Mar. 2010), pp. 176–182.

[17] E. Kim and M. H. W. Chan. "Observation of Superflow in Solid Helium". In: *Science* 305.5692 (2004), pp. 1941–1944.

[18] J.-R. Li et al. "A stripe phase with supersolid properties in spin–orbit-coupled Bose–Einstein condensates". In: *Nature* 543.7643 (Mar. 2017), 91–94.

[19] L. Chomaz et al. "Long-Lived and Transient Supersolid Behaviors in Dipolar Quantum Gases". In: *Phys. Rev. X* 9 (2 2019), p. 021012.

[20] F. Böttcher et al. "Transient Supersolid Properties in an Array of Dipolar Quantum Droplets". In: *Phys. Rev. X* 9.1 (2019), p. 011051.

[21] P. Holzenkamp. "An Optical Dipole Trap with Tunable Geometry for Dysprosium". Bachelors thesis. University of Heidelberg, 2022.

[22] L. Chomaz et al. "Dipolar physics: a review of experiments with magnetic quantum gases". In: *Reports on Progress in Physics* 86.2 (Dec. 2022), p. 026401.

[23] J. R. de Laeter et al. "Atomic weights of the elements. Review 2000 (IUPAC Technical Report)". In: *Pure and Applied Chemistry* 75.6 (2003), pp. 683–800.

[24] E. Poli et al. "Maintaining supersolidity in one and two dimensions". In: *Phys. Rev. A* 104 (6 2021), p. 063307.

[25] J. Hertkorn et al. "Pattern formation in quantum ferrofluids: From supersolids to superglasses". In: *Phys. Rev. Res.* 3 (3 2021), p. 033125.

[26] V. Salazar Silva. "The Accordion Lattice: Towards Trapping of Dysprosium Ultracold Gases in Two Dimensions". Masters thesis. University of Heidelberg, 2023, p. 11.

[27] L. P. Pitaevskij and S. Stringari. *Bose-Einstein Condensation and Superfluidity*. First. International Series of Monographs on Physics 164. Extended and updated version. Oxford: Oxford University Press, 2016, pp. 47–48.

[28] R. N. Bisset. "Theoretical Study of the Trapped Dipolar Bose Gas in the Ultra-Cold Regime". Doctoral dissertation. University of Otago, 2013.

[29] F. Wächtler and L. Santos. "Quantum filaments in dipolar Bose-Einstein condensates". In: *Physical Review A* 93.6 (June 2016).

[30] P. B. Blakie et al. "Compressibility and speeds of sound across the superfluid-to-supersolid phase transition of an elongated dipolar gas". In: *Physical Review Research* 5.3 (Sept. 2023).

[31] A. R. P. Lima and A. Pelster. "Quantum fluctuations in dipolar Bose gases". In: *Phys. Rev. A* 84 (4 2011), p. 041604.

[32] S. Prasad et al. "Instability of Rotationally Tuned Dipolar Bose-Einstein Condensates". In: *Physical Review Letters* 122.5 (Feb. 2019).

[33] T. Fließbach. *Statistical Physics. Textbook on Theoretical Physics IV*. 6th. Berlin: Springer Spektrum, 2018, pp. 354–371.

[34] H. Stoof, D. Dickerscheid, and K. Gubbels. *Ultracold Quantum Fields*. Theoretical and Mathematical Physics. Springer Netherlands, 2008.

[35] T. Gasenzer. *Quantum Field Theory of Many-Body Systems*. Lecture script for the term Winter 2021/22. 2021.

[36] M. L. Chiofalo, S. Succi, and M. P. Tosi. "Ground state of trapped interacting Bose-Einstein condensates by an explicit imaginary-time algorithm". In: *Phys. Rev. E* 62 (5 2000), pp. 7438–7444.

[37] J. Javanainen and J. Ruostekoski. "Symbolic calculation in development of algorithms: split-step methods for the Gross–Pitaevskii equation". In: *Journal of Physics A: Mathematical and General* 39.12 (Mar. 2006), L179–L184.

[38] L. Chomaz, R. van Bijnen, D. Petter, et al. "Observation of roton mode population in a dipolar quantum gas". In: *Nature Physics* 14.5 (2018), pp. 442–446.

[39] P. B. Blakie et al. "Supersolidity in an elongated dipolar condensate". In: *Phys. Rev. Res.* 2 (4 2020), p. 043318.

[40] L. Tanzi et al. "Observation of a Dipolar Quantum Gas with Metastable Supersolid Properties". In: *Phys. Rev. Lett.* 122 (13 2019), p. 130405.

[41] W. Kirkby et al. "Spin rotons and supersolids in binary antidipolar condensates". In: *SciPost Phys. Core* 6 (2023), p. 084.

Acknowledgments

At the end of this thesis, I would like to thank all the people who have supported me throughout the work and without whom this research would not have been possible.

First and foremost, I want to thank Prof. Dr. Lauriane Chomaz for the opportunity to be a part of the Dysprosium Quantum Fluids Group. I gained greatly from her close mentorship and guidance. Thank you for the warm welcome in your group. Your guidance and support where invaluable. I also want to mention that I am looking forward to continue working for you.

Furthermore, I want to thank Wyatt Kirkby for being an incredible supervisor during the last 4 months. For taking the time to answer in much detail my questions regarding physics as well as coding, however small or big they were. Thank you for all your white board explanations as well as being the best desk neighbor one could ask for!

I want to also thank Karthik Chandrashekara for taking the time of explaining the experiment to me and answer all my questions on this end.

Further extending my gratitude to all members of the DysprosiumLab group. You made me feel welcome from the first moment. The relaxing breaks filled with card games motivated enormously.

Special thanks also go to Thomas Gasenzer for kindly being my second examiner.

I acknowledge support by the state of Baden-Württemberg through bwHPC.

Erklärung

Ich versichere, dass ich diese Arbeit selbstständig verfasst und keine anderen als die angegebenen Quellen und Hilfsmittel benutzt habe.

Heidelberg, den 24. Juni 2024,

Lea Maria Luca Neumann